TECHNISCHE UNIVERSITÄT WIEN
Vienna University of Technology

DIPLOMARBEIT

Thermal light tear film imaging with Spectral Domain Optical Coherence Tomography (SD-OCT)

Ausgeführt am

Institut für Angewandte Physik
Technische Universität Wien

unter der Anleitung von

Ao.Univ.-Prof. DI Dr. Martin Gröschl

in Zusammenarbeit mit

Ao.Univ.-Prof. DI Dr. Leopold Schmetterer
Assoc.-Prof. DI(FH) Dr. René Werkmeister

am

Zentrum für med. Physik und Biomedizinische Technik
Medizinische Universität Wien

durch

Iris Schmidt, B.Sc.
Fliederweg 17, 2384 Breitenfurt

Wien, 1. August 2016

Abstract

Determining the morphology and thickness of the tear film of the eye with medical imaging is an important step to improve the diagnosis of dry eye syndrome. Therefore methods have to be developed to enable non-invasive and eye-safe monitoring of this thin layer, measuring only some microns, on the cornea. As a promising approach optical coherence tomography (OCT) has been recently proposed. This light-based, contact-less and label-free technique enables an axial resolution within few microns within an imaging depth range of some millimeters. This combination is optimally suited to image the tear film and the cornea simultaneously.

In this work a low cost line field spectral domain OCT system was designed and constructed which enables the acquisition of a full cross sectional image in one single camera shot without the need to scan laterally. This was realized in a free space setup using a Ti-Sa-Laser with a very high bandwidth up to 300 nm. The chosen components, the adjustment of the setup as well as the data processing are discussed. The measured axial resolution of $3.7 \pm 1.0\,\mu m$ is in good accordance with the theoretical value of $2.4\,\mu m$. Furthermore the lateral resolution along the line could be estimated to be well below $20\,\mu m$. The maximum obtainable sensitivity was approximately 73 dB, mainly limited by high back reflections from planar surfaces of the lenses and optical components in general. Finally, the proper function of the system was demonstrated by successfully resolving the structure of tear film phantoms with thicknesses between 3.26 - 4.81 μm.

Kurzfassung

Die Bildgebung sowie die Dickenbestimmung des Tränenfilms des Auges ist eine wichtige Größe zur besseren Diagnose von trockenen Augen. Da dieser Film jedoch nur wenige Mikrometer dick ist, müssen zunächst Methoden entwickelt werden, die hochauflösend und nichtinvasiv zugleich sind. Die rasante Entwicklung der optischen Kohärenztomographie (OCT) innerhalb der letzten Jahre macht dieses Verfahren zu einem vielversprechenden Kandidaten für diese Problemstellung. OCT ist ein optisches, kontaktfreies und vor allem farbstofffreies Bildgebungsverfahren, welches eine axiale Auflösung weniger Mikrometer über einen Messbereich von bis zu einigen Millimetern erreicht. Es ist damit ein optimales Werkzeug um den Tränenfilm und die Cornea gleichzeitig bildgeben zu können.

In der vorliegenden Arbeit wurde ein preiswertes line field Spektrometer basierendes OCT System entworfen und aufgebaut, welches die Aufnahme eines gesamten Schnittbildes mit einer einzigen Kameraaufnahme ohne laterales Scannen ermöglicht. Dies wurde in einem Freifeld-Aufbau auf dem optischen Tisch realisiert, wobei als Lichtquelle ein Ti-Sa-Laser mit einer Bandbreite von bis zu 300 nm eingesetzt wurde. Die eingesetzten Komponenten, die Justierung des Systems sowie die nachträgliche Datenprozessierung zur Berechnung des Schnittbildes werden diskutiert. Die gemessene axiale Auflösung lag bei $3.7 \pm 1.0\,\mu m$ und ist in gutem Einklang mit dem theoretisch erwarteten Wert von $2.4\,\mu m$. Die laterale Auflösung entlang der Linie konnte auf unter $20\,\mu m$ abgeschätzt werden. Die maximale Empfindlichkeit betrug 73 dB, was vorwiegend auf die starken Rückreflektionen der optischen Komponenten, insbesondere der planen Oberflächen der Linsen, zurückzuführen war. Zu guter Letzt wurde die Leistungsfähigkeit des Systems demonstriert, indem Tränenfilmphantome mit Dicken von $3.26 - 4.81\,\mu m$ erfolgreich gemessen werden konnten.

Acknowledgements

First of all, I want to thank my thesis advisors Martin Gröschl, Leopold Schmetterer and René Werkmeister for giving me this amazing opportunity and support. With special thanks to René for always being helpful, providing me knowledge and advice.

Moreover, thanks to my working group, especially to Sophie, Gerold, Martin V., Veronika, Jozsef, Valentin, Christian, Martin P., Alina and Thomas for the fruitful discussions, motivating conversations and basically for having always a sympathetic ear. And thank you, for sharing not only professional interests but also becoming friends. The first among these is Sophie. I appreciate a lot that I found in Sophie not only a marvelous and enriching colleague but also a good friend with a wonderful positive attitude - "Take it easy, be happy."

Many other colleagues contribute to my thesis by lending me components and their time for discussing problems whenever I needed it, sharing helpful ideas and giving words of cheer and motivation as well as by providing help with the organisational and practical matters. Amongst them are the scientists Angelika, Marco, Matías, Michael, Daniel, Menyang, Abhishek, Pablo and Simon as well as the staff at the ZMPBMT, including Andi, Peter, Bernhard, Sigi, Harald, Jutta, Melitta, Angela and many more. Thank you all.

Thanks to all colleagues who have motivated and inspired me during my master thesis, especially to my PhD colleagues who have adopted me to their PhD-Get-Togethers even before I am holding a master's degree.

My gratitude goes as well to my non-OCT-friends, whom I have known for a long time. Thank you for patiently listening to me talking about my master thesis for hours on end, spending great times together, the possibility to share all up and downs and being there whenever I need you. You are the best imaginable friends.

Last but not least, special thanks go to my family, especially my parents, who offered me the chance to study physics, always provided me support and give me lots of love.

Contents

List of Figures

List of Tables

List of Abbreviations

DOF	depth of focus
FD-OCT	Fourier domain optical coherence tomography
FFT	fast Fourier transform
FWHM	full width at half maximum
LF-FD-OCT	line field Fourier domain optical coherence tomography
LF-SD-OCT	line field spectral domain optical coherence tomography
MPE	maximum permissible exposure
NA	numerical aperture
NDF	neutral density filter
NIR	near infrared
OCT	optical coherence tomography
SLD	superluminescent diode
SNR	signal-to-noise ratio
Ti-Sa-Laser	Titanium Sapphire Laser
TD-OCT	time domain optical coherence tomography

Chapter 1

Introduction and Motivation

Dry eye syndrome (DES) is a common disease in the present with a sight-threatening potential [2] on long term. Nowadays people are often working with computers and are therefore watching screens for many hours per day which is causing a higher potential for DES. As for the causes of this pathology it seems that the dryness of the cornea is directly correlated to tear film instability. Nevertheless, in general DES remains difficult to diagnose properly due to the weak association between symptoms and objectively measurable signs [3].

To adequately measure the morphology of the tear film as for example the thickness, measurement modalities able to resolve this thin layer have to be considered. So far, some invasive methods have already been developed with poor reproducibility and rather low resolution ([4, 5]). First non-invasive techniques in the early and late nineties, e.g. confocal microscopy and interferometry, resulted in measured tear film thickness values in very broad range spreading from around 3 up to 46 µm ([6, 7]). Since the development of high resolution optical coherence tomography (OCT) and the progress in the development of broadband light sources, there has been a big step forward to the direct measurement of the tear film thickness with high accuracy and precision ([8–10]). OCT is a non-invasive optical imaging modality with high axial resolution up to few microns and enabling penetration depths around 1 to 2 mm depending on the tissue of interest. By use of a broadband Ti-Sa-Laser ($\lambda_0 = 800$ nm, FWHM = 170 nm) Werkmeister et al. [11] achieved a theoretical axial resolution of 1.2 µm in the cornea and measured an average central tear film thickness of 4.79 ± 0.88 µm which show the great potential of tear film imaging with OCT. This is in good accordance with the thickness range of $3.0 - 6.3\,\mu m$ measured with OCT by Yadav et al. [9] and Kottaiyan et al. [10].

This thesis aims to further improve the axial resolution for potential OCT-based tear film imaging by using an Ti-Sa-Laser with an even larger bandwidth of FWHM = 300 nm along with a central wavelength $\lambda_0 = 800$ nm. The OCT setup is designed with a line field illumination ([12, 13]) and a low cost camera enabling cross-sectional images of the

sample of interest in one single shot. This reduces significantly the costs as fast scanning systems for lateral deflection as currently used in standard point-scanning OCT can be omitted. In addition this technique called line field spectral domain OCT (LF-SD-OCT) allows a higher optical power entering the eye within the safety regulations (see chapter 3.3.6) as regular OCT systems allowing better signal quality.

In this thesis a LF-SD-OCT system was designed according to the specifications required for potential tear film imaging. It was then constructed using commercially available standard components keeping the low cost character of the technique in mind. Finally the proposed setup was characterized regarding sensitivity and resolution and compared to the theoretically expected values as well as validated by the measurement of tear film phantoms.

Chapter 2

Principle of Optical Coherence Tomography

Optical coherence tomography (OCT) is a contactless optical imaging technique, which is used to measure depth profiles of diaphanous scattering media. By this means, information about the sample structure can be obtained non-invasively. As a consequence, OCT has become a standard diagnosis tool in ophthalmology.
It is based on low coherence interferometry, which uses low coherence light (i.e. broad bandwidth light) to illuminate a sample in a Michelson interferometer. The resolution in OCT is determined by the coherence length of the light which is inversely proportional to the spectral bandwidth.

2.1 The Michelson Interferometer

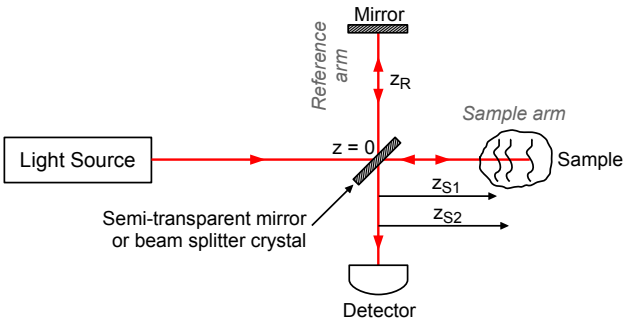

Figure 2.1: Schematic drawing of a Michelson interferometer (adapted from [14], page 71). Most OCT setups are based on a Michelson interferometer.

OCT systems are usually based on a Michelson interferometer (see figure 2.1). The light from the source is splitted by a beam splitter into the sample arm and the reference arm,

respectively. The reflected and backscattered light from the sample and the reference mirror interferes in the detection arm and is captured by a detector.

Interference may be detected, if the optical path length difference between both interferometer arms is smaller than the coherence length of the light source. Hence, the intensity I_D at detector is given by

$$I_D \propto |E_R|^2 + |E_S|^2 + 2E_R E_S \cos(2k\Delta L). \tag{2.1}$$

The first two terms occur even if no interference exists. But the last term exists only in case of interference and depends on the path length difference between both arms $\Delta L = 2z_R - 2z_S$. Subsequently, by measuring the intensity I_D and with the knowledge of the reference arm length, the distance of the reflecting sample layer can be determined.

2.2 Mathematical basics of OCT

A detailed mathematical explanation of OCT is given by Izatt and Choma ([14], chapter 2). A summary of the basic idea and the results is given in the following.

In the interferometer a light wave with an electric field E_i is incident

$$E_i = s(k,\omega)\mathrm{e}^{i(kz-\omega t)}, \tag{2.2}$$

where $s(k,\omega)$ is the amplitude, $(kz - \omega t)$ the phase of the incident electric field, z the spatial coordinate along the axial direction, k the wave vector, ω the angular frequency and t the temporal coordinate.

In an OCT setup (as shown in figure 2.1), the beam splitter is located at $z = 0$ and divides the incident beam into two paths. One part propagates toward the reference mirror and the back reflected electric field is given by

$$E_R = \frac{s(k,\omega)}{\sqrt{2}} \cdot r_R \cdot \mathrm{e}xp\,(i(-kz - \omega t + \phi_R)), \quad \phi_R = 2kz_R - \pi \tag{2.3}$$

where r_R is the reflectivity of the reference mirror which is located at z_R and ϕ_R is an additional phase shift caused by the optics in the reference arm. The factor $1/\sqrt{2}$ arises from the beam splitter which is equally distributing the intensity (and not the amplitude) in both arms.
Similarly, the other wave propagates in the sample arm. The sample is located at z_S and assumed to be composed of several discrete reflecting layers at the positions z_{S_n}. This yields a sample reflectivity of $r_S(z_S) = \sum_n r_{S_n}\delta(z_S - z_{S_n})$, where δ denotes the dirac distribution function. Thus the electric field of the reflected sample wave is given by

$$E_S = \frac{s(k,\omega)}{\sqrt{2}} \sum_n r_{S_n}\, \mathrm{e}xp\,(i(-kz - \omega t + 2kz_{S_n} - \pi)). \tag{2.4}$$

Back at the beam splitter, the two beams are superimposed and captured on the detector. Based on the fact, that for every available detector the rate of detection is much smaller than the frequency ω, the interference signal is already time averaged (notation$\langle\rangle$) while measuring. The detected beam intensity is given by

$$I_D(k,\omega) = |E_D|^2 = \frac{\rho}{2}\langle|E_R + E_S|^2\rangle, \tag{2.5}$$

where ρ is the detector response.
By introducing the light source spectrum $S(k) = \langle|s(k,\omega)|^2\rangle$ and the power reflectivity $R = |r|^2$ as well as applying some minor mathematical operations equation 2.5 can be rewriting as

$$\begin{aligned} I_D(k) = &\frac{\rho}{4}S(k)\cdot\left(R_R + \sum_n R_{S_n}\right) + \\ &+ \frac{\rho}{2}S(k)\cdot\sum_n \sqrt{R_R R_{S_n}}\cdot\cos\left(2k(z_R - z_{S_n})\right) + \\ &+ \frac{\rho}{4}S(k)\cdot\sum_{n\neq m} \sqrt{R_{S_n} R_{S_m}}\cdot\cos\left(2k(z_{S_n} - z_{S_m})\right). \end{aligned} \tag{2.6}$$

The terms in the first line are the so called DC terms, the ones in the second line the cross-correlation terms and the last line contains the auto-correlation terms. Izatt and Choma ([14], chapter 2, page 74) describe these terms as:

1. *DC-terms*: A path length-independent offset to the detector current, scaled by the light source wavenumber spectrum and with amplitude proportional to the power reflectivity of the reference mirror plus the sum of the sample reflectivities. This term is often referred to as "constant" or "DC" component. This is the largest component of the detector current if the reference reflectivity dominates the sample reflectivity.
2. *Cross-correlation terms*: A "cross-correlation" component for each sample reflector, which depends upon both light source wavenumber and the path length difference between the reference arm and sample reflectors. This is the desired component for OCT imaging. Since these components are proportional to the square root of the sample reflectivities, they are typically smaller than the DC component. However, the square root dependence represents an important logarithmic gain factor over direct detection of sample reflections.
3. *Auto-correlation terms*: "Auto-correlation" terms representing interference occurring between the different sample reflectors appear as artefacts in typical OCT system designs [...]. Since the autocorrelation terms depend linearly upon the power reflectivity of the sample reflections, a primary tool for decreasing autocorrelation artefacts is selection of the proper reference reflectivity so that the autocorrelation terms are

small compared to the DC and interferometric terms (Izatt and Choma [14], chapter 2, page 74).

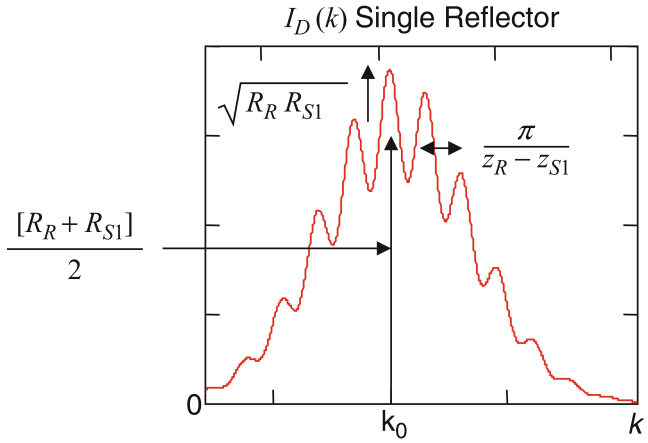

Figure 2.2: Schematic drawing for $I_D(k)$ for a single reflector([14], chapter 2)

In case of a single reflector, the detected $I_D(k)$ consists only of a DC term (maximum height proportional to $\frac{R_R+R_{S1}}{2}$) overlayed with a cosinusoidal modulation origin from the cross-correlation term (height proportional to $\sqrt{R_R R_{S1}}$, see schematic in figure 2.2). Neither further cross-correlation nor auto-correlation terms are present in the case of a single reflector in the sample arm.
If the sample has several reflecting layers, the detected $I_D(k)$ would be additionally modulated by several cross-correlation and auto-correlation terms.

2.3 Time domain OCT vs. Fourier domain OCT

All OCT systems are either based on time domain optical coherence tomography (TD-OCT) or on Fourier domain optical coherence tomography (FD-OCT).

In **TD-OCT** a broadband light source with low coherence is used (see figure 2.3). Interference occurs only if the optical path lenght of the sample arm is equivalent to the optical path length of the reference arm plus or minus the narrow coherence length. By moving the reference mirror along the axis of the reference arm different depths of the sample are scanned. The intensity recorded over depth of a point at the sample displays a reflectivity depth profile the so called A-Scan. The drawback of TD-OCT is that moving the reference mirror is time costly which can be overcome by the use of FD-OCT.

In **FD-OCT**, a broadband interference signal is spectrally resolved and the depth scan is obtained by Fourier transforming the signal, thus acquiring one depth scan without

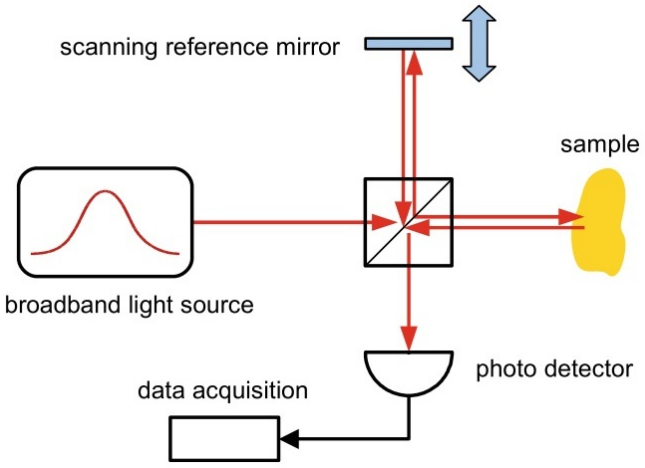

Figure 2.3: In time domain optical coherence tomography (TD-OCT) a depth scan is performed by shifting the reference mirror along the axis of the reference arm [15]

moving any components. FD-OCT can be further classified by the way of detection as spectrometer based and swept source (SS) based.
A spectrometer-based system uses a broadband light source and the interference signal is spectrally resolved by a diffraction grating, i.e. the grating disperses the signal in accordance to its frequency components (for details see the theory of the diffraction grating in appendix A)). Following this, the signal is imaged by an 1-D CCD array (see figure 2.4).

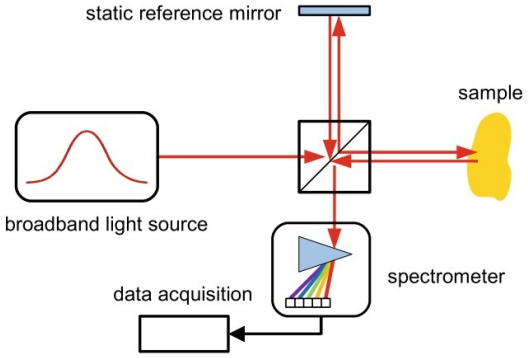

Figure 2.4: Spectrometer-based Fourier domain optical coherence tomography (FD-OCT) with a broadband light source ([15], page 2701)

A swept source-based system uses a tunable narrowband light source, which changes the frequency of the narrow spectral bandwidth in time. Hence here is no need of an 1-D detector, because the interference can be detected by a photodiode (see figure 2.5).

In all FD-OCT systems the detected intensity spectrum contains the information of different sample depths without the need to scan along the axial direction. The intensity spectrum is spectrally resolved detected and has to be Fourier transformed in order to ob-

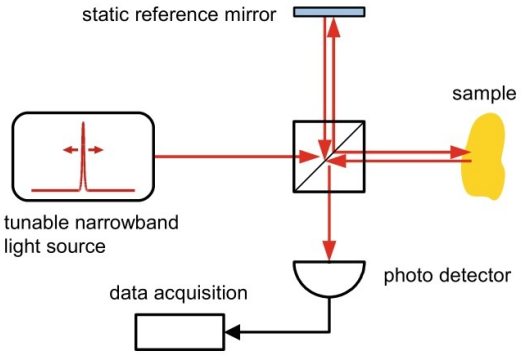

Figure 2.5: Swept source-based FD-OCT with a tunable narrowband light source ([15], page 2701)

tain the depth-resolved reflectivity profile (A-scan) of the imaged sample.
Additionally, FD-OCT is not only faster than TD-OCT but also has a sensitivity advantage of 20 - 30 dB over conventional TD-OCT proved by Leitgeb et al. [16] and Choma et al. [17].

Already from equation 2.1 it is possible to conclude that larger differences in path length lead to higher frequencies of the modulations in the interference signal. Multiple layers in depth cause several interference frequencies. By Fourier transforming the measured detector current $I_D(k)$, the depth information $i_D(z)$ is decoded

$$i_D(z) = \mathcal{F}(I_D(k)) \tag{2.7}$$

which results (according to [14], chapter 2) in

$$\begin{aligned} i_D(z) = \frac{\rho}{4}\gamma(z) \cdot \Big(R_R + \sum_n R_{S_n}\Big) + \\ + \frac{\rho}{4} \sum_n \sqrt{R_R R_{S_n}}\,[\gamma(z + 2(z_R - z_{S_n})) + \gamma(z - 2(z_R - z_{S_n}))] + \\ + \frac{\rho}{8} \sum_{n \neq m} \sqrt{R_{S_n} R_{S_m}}\;\; [\gamma(z + 2(z_{S_n} - z_{S_m})) + \gamma(z - 2(z_{S_n} - z_{S_m}))]. \end{aligned} \tag{2.8}$$

Similar to equation 2.6, the first line belongs to the so called DC terms, the second line to the cross-correlation terms and the last line contains the auto-correlation terms.

Hence, the Fourier transform of a recorded wavelength spectrum yields a depth profile (A-scan) which is displaying all frequencies of the detected interference signal by single peaks (see figure 2.6). Different frequencies refer to different reflecting sample layers z_{Sn}. By analysing the positions of the cross-correlation frequency components, the absolute positions of the sample layers can be determined.
Due to the symmetry of the cosine in equation 2.6, the cross correlation as well as auto correlation terms appear twice and symmetric around z=0. In figure 2.6, all peaks to the left of the DC term are chosen to be the signal of interest. The remaining peaks on the other side of the DC term contain the same information, thus they are called mirror image

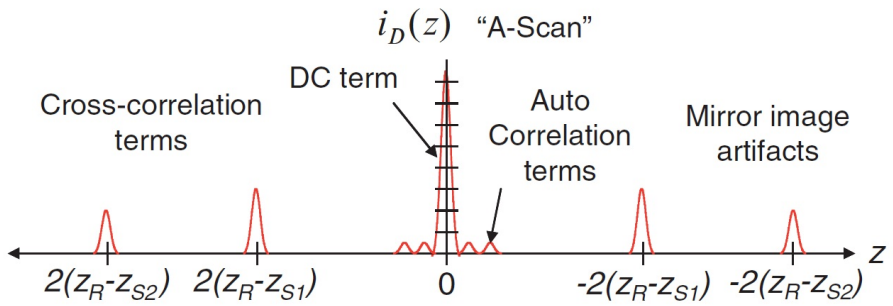

Figure 2.6: Depth profile (A-scan) of a sample with two layers at z_{S1} and z_{S2} and the reference mirror is located at z_R ([14], chapter 2).

artifacts and can be neglected.

The major advantage of FD-OCT is obtaining the whole depth information (A-scan) in one single measurement. That is why it is acquiring faster than TD-OCT and nowadays the method of choice.

2.4 Line field OCT

In normal OCT only a point is illuminated at the sample, hence it is necessary to scan in two lateral directions. In contrast, in line field spectral domain optical coherence tomography (LF-SD-OCT), the sample is illuminated by a line and the reflected as well as backscattered light is captured by a two-dimensional (2D) detector. In order to scan an area on the sample it is sufficient to scan in one direction. As a consequence, LF-OCT is able to image significantly faster.

A depth profile measured at a single point is the so called A-scan. Similar a B-scan is a two-dimensional tomogram which is obtained by acquiring A-scans while scanning in a lateral direction (in the case of a point scanning system). In LF-SD-OCT a whole B-scan is obtained with one camera shot.

The enhancement in imaging speed by using line illumination as well as the sensitivity advantage of FD-OCT over TD-OCT, as already mentioned in chapter 2.3, have lead to the development of LF-SD-OCT.

A typical LF-SD-OCT setup is based on a Michelson interferometer using a broadband light source and an anamorphic illumination system in order to illuminate the sample and the reference mirror with a line. The back reflected light is reunited at the beam splitter and the so caused interference signal is dispersed by a diffraction grating. Subsequently, the spectrally resolved interference signal is detected by an CCD or CMOS area camera.

Hence, depth profiles for each point along the line can be obtained in parallel.

In 1999, one of the first LF-FD-OCT was build and tested on a technical sample by Zuluaga and Richards-Kortum [18]. Six years later, the first demonstration of LF-FD-OCT achieving in vivo tomograms of the human eye (especially of the anterior chamber, iris and cornea) was performed by Grajciar et al. [1] (see figure 2.7). With a superluminescent diode (SLD) light source ($\lambda_0 = 811$ nm, FWHM = 17 nm) axial and lateral resolutions of 17 nm and 100 nm, respectively, were obtained. Moreover, the detected sensitivity was 89 dB with 2 mW power on the sample.

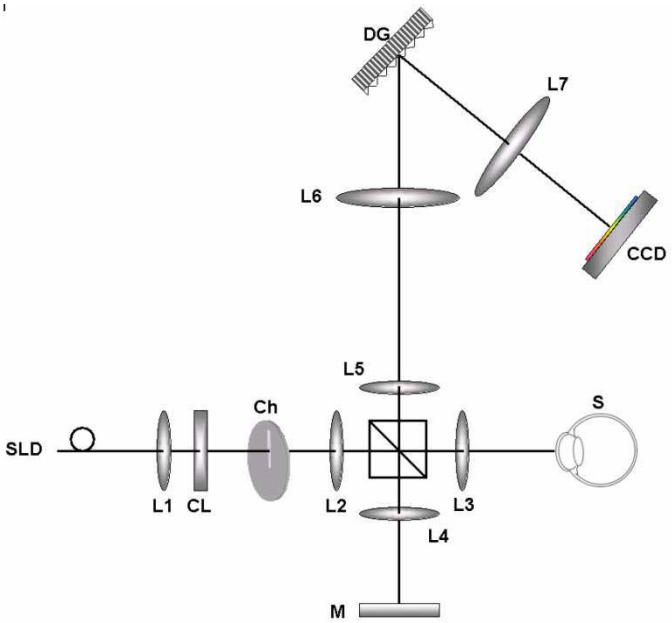

Figure 2.7: Schematic of the LF-FD-OCT system demonstrated by Grajciar et al. [1]

Other approaches in Line field OCT were performed as well. For example a LF-SD-OCT setup was combined with adaptive optics as demonstrated by Zhang et al. [19]. The adaptive optics is correcting aberrations (e.g. astigmatism), thus leading to a significant improvement in sensitivity of about 11.4 dB. Another approach is using a frequency-sweeping laser with a high speed camera. This not only simplifies the imaging optics, but also avoids spectral cross-talk with which LF-SD-OCT has to deal with ([12], [13]).

Chapter 3

Methods and Materials - The OCT Setup and its Specifications

3.1 The light sources

The discussed line field setup was planned for a Titanium Sapphire Laser (Ti-Sa-Laser) with a central wavelength of about $\lambda_0 = 800\,\text{nm}$ and a spectral bandwidth of approximately 300 nm (see Fig. 3.1).

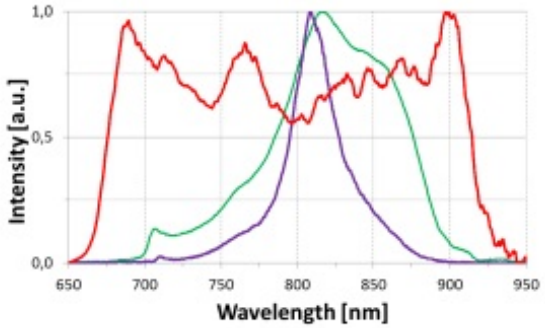

Figure 3.1: The red cure shows the spectrum of the used Ti-Sa-Laser (measured by Angelika Unterhuber, ZMPBMT, Medical University of Vienna).

During the alignment process of the OCT setup the Ti-Sa-Laser was not available due to technical issues. Hence, another light source in stock, a superluminescent diode, the Superlum SLD (BroadLighter-T840, Superlum Diodes Ltd., Carrigtwohill, Ireland), was used for aligning the setup. Its central wavelength is about 40 nm longer than the one of the initial planned Ti-Sa-Laser. According to the manufacturer, the Superlum SLD has a central wavelength of $\lambda_0 = 840\,\text{nm}$ and a bandwidth of 100 nm. The measured spectrum of the Superlum SLD shows a central wavelength of $\lambda_0 = 841.8\,\text{nm}$ and a bandwidth of

99.5 nm (see figure 3.2). The spectrum of the Superlum SLD was measured by placing the probe of a high-resolution spectrometer (HR2000CG-UV-NIR, Ocean Optics, Dunedin, Florida, USA) in the focus of the sample plane.

For performing measurements with a higher axial resolution than obtainable with the Superlum SLD, a Ti-Sa-Laser with other spectral properties than the initial planned one was used (see figure 3.2). Its spectrum was measured with the same high-resolution spectrometer by placing the probe at the Laser output before coupling into a fiber leading to the OCT setup. The so obtained spectrum has a central wavelength of $\lambda_0 = 740.5$ nm and a bandwidth of approximately 136.7 nm.

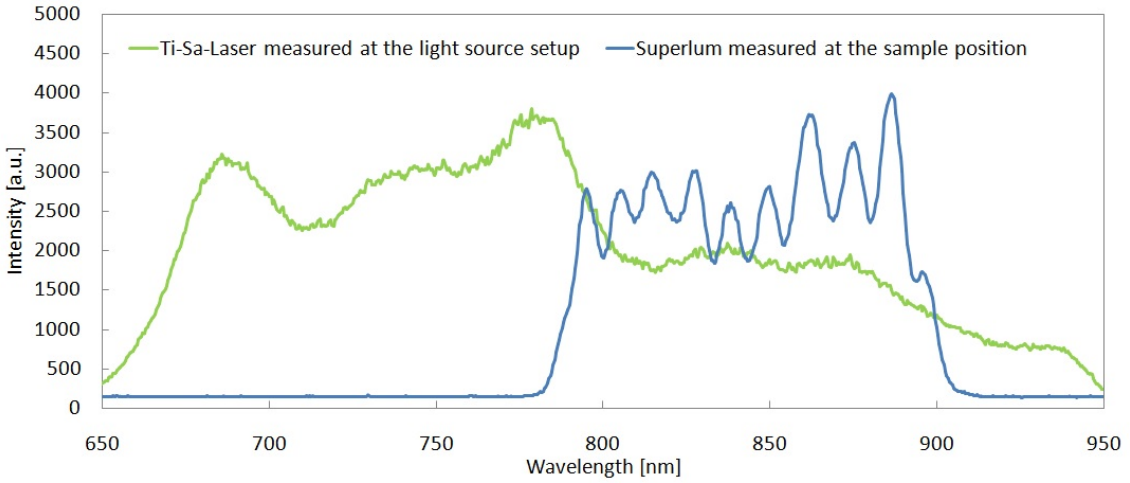

Figure 3.2: These are the spectra used for the measurements performed in chapter 4. The green line shows the spectrum of the Ti-Sa-Laser at its output. The blue line corresponds to the spectrum of the Superlum SLD measured at the sample position. The spectra were measured with a high-resolution spectrometer (HR2000CG-UV-NIR, Ocean Optics, Dunedin, Florida, USA)

The output power from the Ti-Sa-Laser is 65 mW before coupling into the fiber. The Ti-Sa-Laser output is connected with the OCT setup by three fibers in a row with an overall length of about 20 m. A power of 8.2 mW is coupled into the OCT system. The transfer losses are probably caused by the long fiber and the two couplings between the Ti-Sa-Laser output and the OCT setup.

The whole OCT setup was aligned with the Superlum SLD except the line field spectrometer and the dispersion compensating prism pair. These two components were expected to be very wavelength-dependent and therefore they were adjusted with the finally used Ti-Sa-Laser.

3.2 Line up of the setup

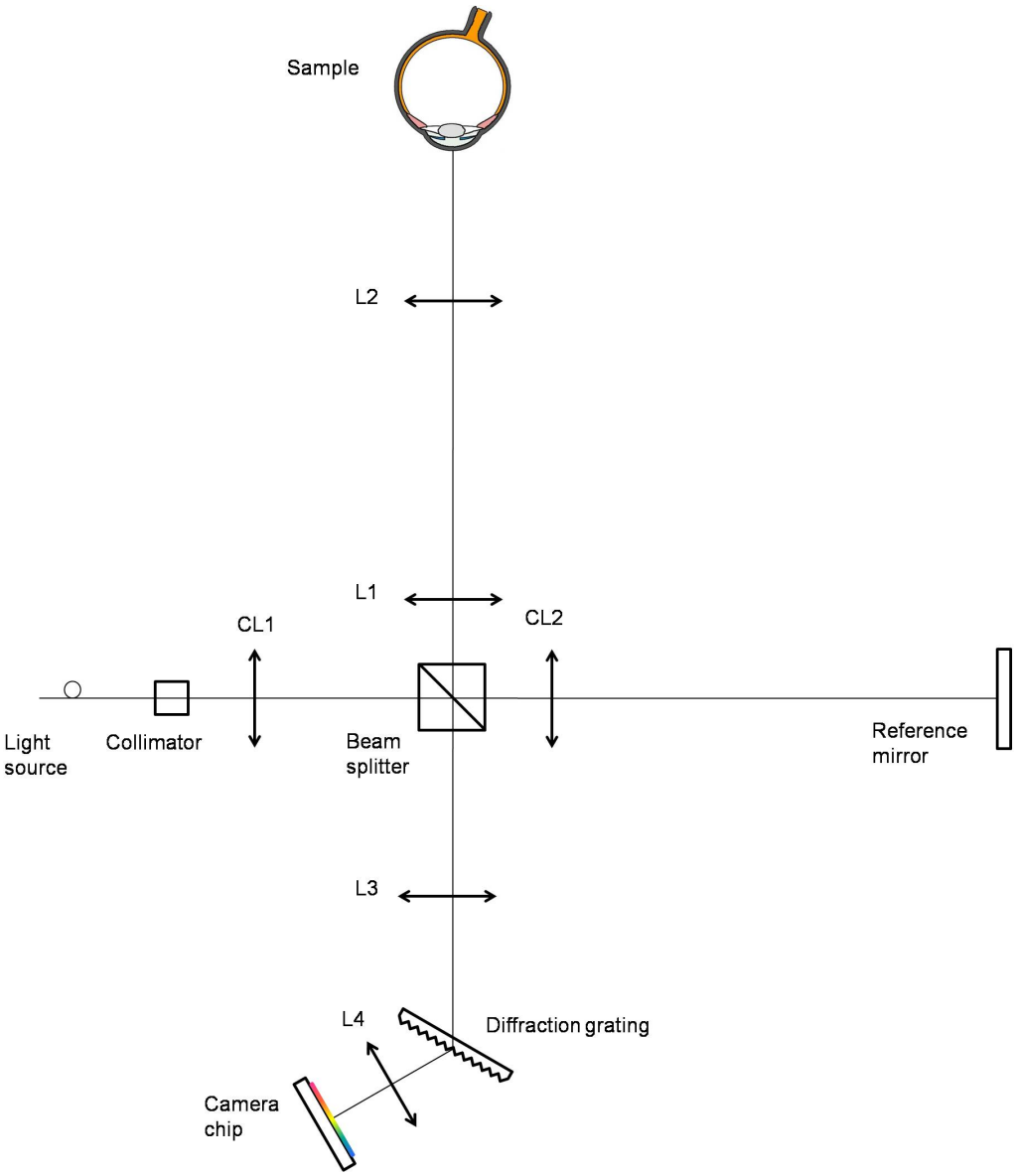

Figure 3.3: The schematic of the LF-FD-OCT system. CL1, CL2 cylindrical lenses f=75mm; non-polarizing beam splitter 70:30 (reference : sample arm); L1 - L3 achromatic lenses f=75mm; diffraction grating; L4 achromatic lens f=30mm

The setup discussed in this thesis is planned similiar to the line field setup of Grajciar et al. [1]. The line field Fourier domain optical coherence tomography (LF-FD-OCT) system of the project thesis is schematically drawn in figure 3.3. The horizontal and vertical perspectives of the optical path are given in figure 3.4. The system is divided by the non-polarizing beam splitter (splitting ratio 70:30 of reference : sample arm) in four optical arms. The illumination arm, the sample arm, the reference arm and the detection arm. For details of the optical components see table 3.1.

In the illumination arm, the light intensity can be adapted by a variable neutral density filter (NDF, 50FS02DV.2, Newport, CA, USA). It is followed by the cylindrical lens CL1 which causes the line illumination. This line is imaged by a Rayleigh lens pair (achromatic lenses L1 and L2) onto the sample. The horizontal plane is similar to a point illumination FD-OCT setup. In the vertical plan the LF-FD-OCT setup differs from one with point illumination. Because of the line illumination, all points along the line are imaged at once and there is no need of scanning the sample in the vertical direction.

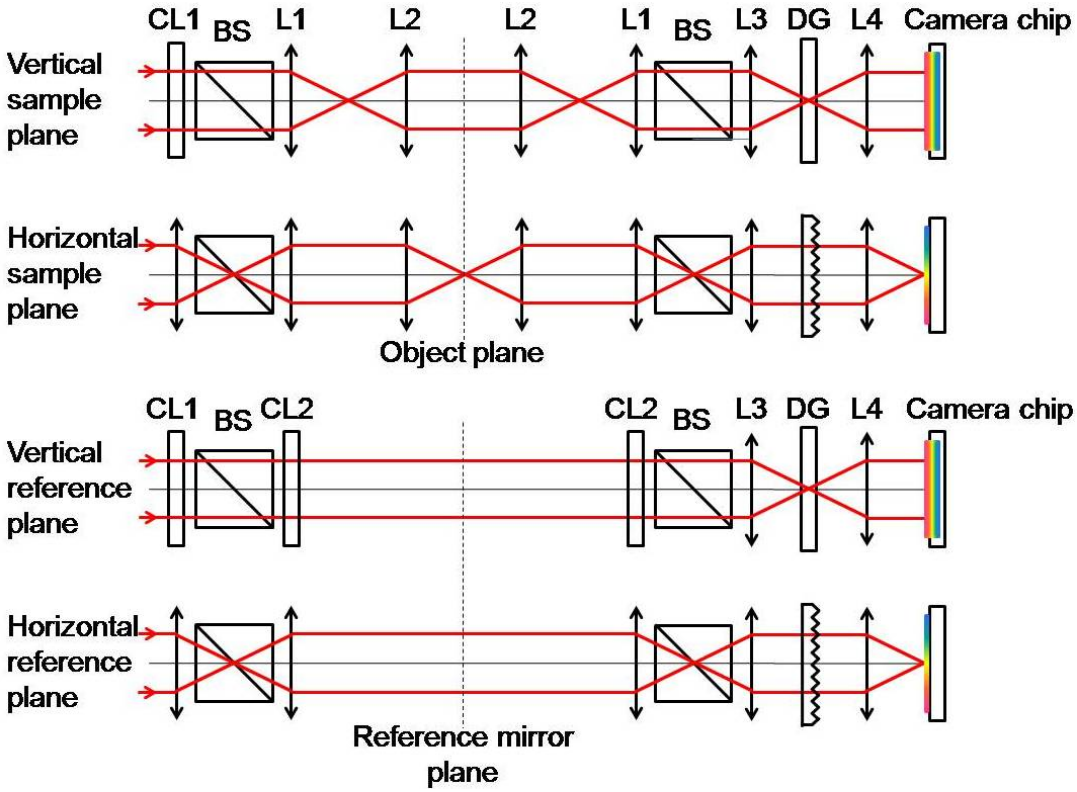

Figure 3.4: Horizontal and vertical perspectives of the optical path of the LF-FD-OCT system. The abbreviations are the same as in figure 3.3

In the reference arm the beam is collimated by the cylindrical lens CL2. A variable neutral density filter (NDF, 50FS02DV.2, Newport, CA, USA) is placed in the collimated beam between CL2 and the reference mirror in order to enable adapting the power of the ref-

erence arm to the sample arm. Moreover, a glass prism pair, made of BK7 (borosilicate crown glass, Schott) and joined with an index-matching fluid, is induced as well. The dispersion mismatch between both arms can be matched by shifting the prisms relatively to each other. The reference mirror is mounted on a translation stage which can be shifted for changing the length of the reference arm (see figure 3.5).

The beam reflected from the sample is reunited with the beam of the reference arm and imaged to the diffraction grating. The dispersed beam is imaged by the achromatic lens L4 to the camera chip. The area camera based on a CMOS sensor detects the spectrally resolved interference signal.

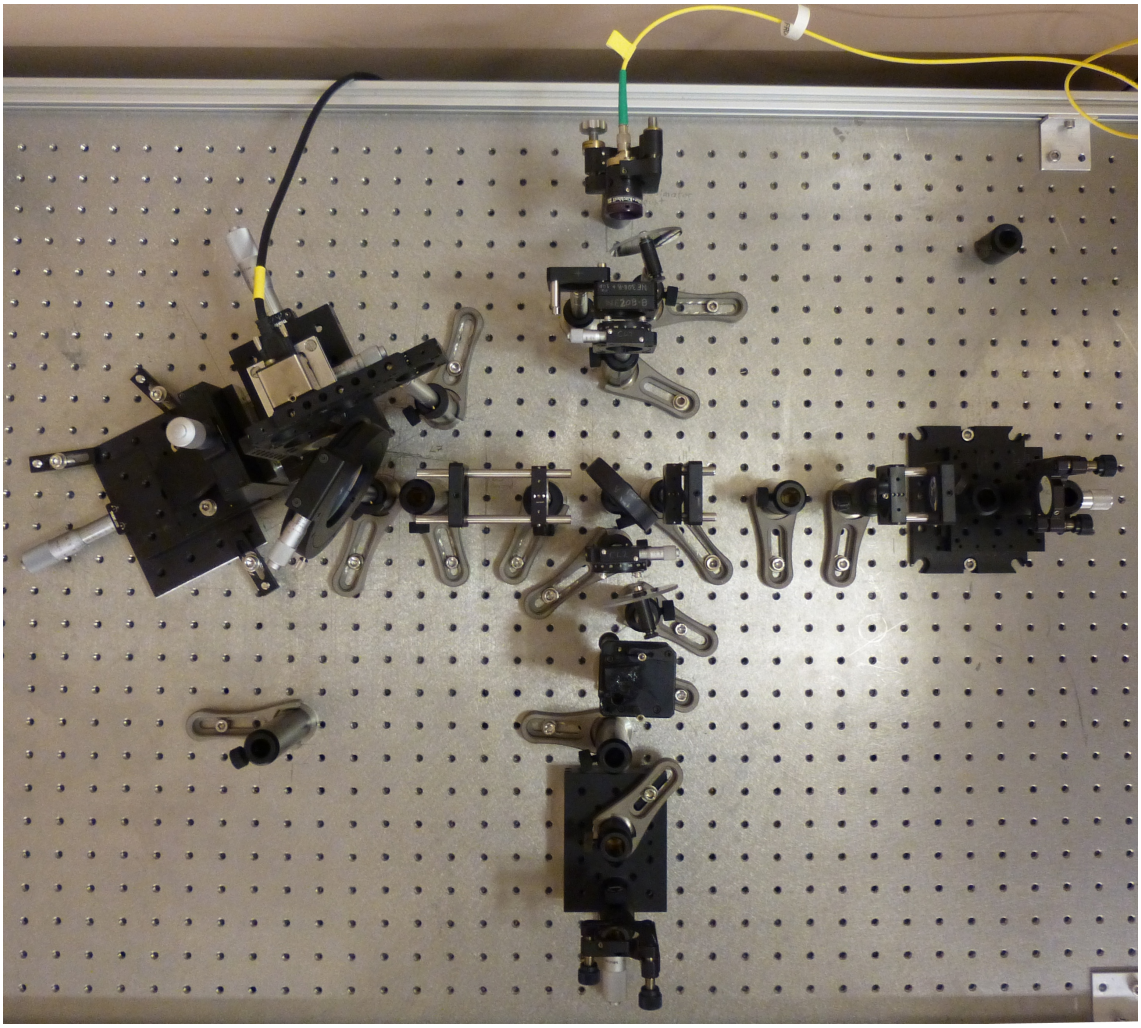

Figure 3.5: Topview of the optical setup: The beam splitter (BS) is located in the centre. Above the BS the illumination arm and below the reference arm are located. On the right side lies the sample arm (measuring the sample mirror at that moment). On the left side of the BS the light travels through the detection arm imaging the interference signal on the spectrometer.

The sample plane and the camera chip plane are conjugated image planes to each other,

while the diffraction grating is in a Fourier plane of the sample plane. This condition fulfils the requirement that along the same direction the beam focused on the sample (i.e. horizontal plane in this setup) it must be collimated at the diffraction grating in order to be correctly dispersed by the last named. Subsequently, the spectrally resolved signal is focused on the camera chip plane.

When we first built the setup, the spectrometer was built as initially planned with a reflection grating (see appendix B). In this configuration it was recognized, that unlike the calculation in chapter B.1.2 the length of the line at the grating exceeded the horizontal dimension of the grating. Hence, only a very small sensitivity of 66 db was obtained with the Ti-Sa-Laser. Overall, the spectrometer was redesigned and a transmission diffraction grating was chosen (for details see chosen components in table 3.1).

Table 3.1: List of the components used in the optical setup as well as their acronyms and manufacturer product codes

Acro.	**Part specification**	**Product No.**	**Company**
COL	Fiber collimator, f = 30 mm, focusable, ARC 650 - 1050 nm, NA 0.19	60FC-T-4-M30-02	Schäfter + Kirchhoff
CL1, CL2	Cylindrical Achromatic Doublets, ARC 650 - 1050 nm	ACY254-075-B	Thorlabs
L1, L2, L3	Achromatic Doublet, f = 75mm, ARC 650 - 1050 nm	AC254-075-B	Thorlabs
L4	Achromatic Doublet, f = 30mm, ARC 650 - 1050 nm	AC254-030-B	Thorlabs
BS	UVFS Plate Beamsplitter 30:70 (R:T), D = 2”, ARC 700 - 1100 nm	BSS17	Thorlabs
DG	Transmission diffraction grating 1200 l/mm, blazed at 840 nm, ARC 740 940 nm	WP-1200/840-50.8	Wasatch Photonics
CAM	Area camera based on CMOSIS Sensor, 2048 x 1088 pixel, USB 3.0	UI-3360CP-NIR	IDS Imaging Developtment Systems

3.3 System parameters

The theoretical setup's accuracy and performance is defined by several parameters which are given in the following. They are based on the spectrum of the light source (Ti-Sa-Laser) used for the measurements discussed in chapter 4 (see figure 3.2).

The final spectrometer was planned for the former spectrum of the Ti-Sa-Laser (see figure 3.1) which had a broader bandwidth than the spectrum of the configuration that was later used for the measurements. Hence, the setup would have performed better with the broader spectrum in terms of axial resolution than with the spectrum of the Ti-Sa-Laser in the current case.

3.3.1 Imaging depth and image resolution along the axial direction

The detected intensity depends on a path length difference between the reference and the sample arm. The bigger the difference is, the faster the detected intensity oscillates. The maximum measurable imaging depth z_{max} is limited by the ability of resolving high spatial frequencies by the camera and should not be confused with the penetration depth into the sample, which describes the maximum sample depth from which the back scattered signal is still strong enough to be detected. By use of the Nyquist criterion the maximum imaging depth of a depth scan (A-scan) is given by ([14], page 83):

$$\pm z_{max} = \pm\frac{\pi}{2 \cdot \delta_s k} = \pm\frac{\lambda_0^2}{4 \cdot \delta_s \lambda}, \tag{3.1}$$

where λ_0 is the central wavelenght of the light source and $\delta_s\lambda$ decribes the spectral difference between two adjacent pixels (i.e. spectral resolution). However, this equation only applies in vacuum. In a medium, the refractive index n has to be taken into account because instead of geometrical lengths, optical paths lengths are measured. This leads to a sampling depth of

$$\pm z_{max} = \pm\frac{1}{n}\frac{\lambda_0^2}{4 \cdot \delta_s \lambda}. \tag{3.2}$$

The spectral sampling width of the camera chip $\delta_s\lambda$ is given by

$$\delta_s\lambda = \frac{\Delta\lambda}{N}, \tag{3.3}$$

where $\Delta\lambda$ is the maximum spectral bandwidth detectable by the camera and N the number of pixels along the horizontal direction.
The camera used in this setup has 2048 pixel along the horizontal direction. Moreover, the minimum and maximum wavelengths recordable on the camera are calculated (according to figure B.1) to be 665 nm and 938 nm, respectively. Consequently, $\delta_s\lambda$ is

$$\delta_s\lambda = \frac{938\,\text{nm} - 665\,\text{nm}}{2048} = 0.133\,\text{nm}. \tag{3.4}$$

In the final setting of the Ti-Sa-Laser, with which the measurements in chapter 4 were obtained, the central wavelength is (according to figure 3.2) $\lambda_0 = 740.5\,\text{nm}$. This leads to a maximal imaging depth in vaccum of

$$z_{max} = \frac{740.5\,\text{nm}^2}{4 \cdot 0.133\,\text{nm}} = 1.03\,\text{mm}. \tag{3.5}$$

The measured coatings of the tear film phantoms have a refractive index n of 1.62 in the wavelength region 740 - 840 nm. Thus, the maximum imaging depth is reduced to $\Delta z_{max} = 0.63\,\text{mm}$ when measuring the tear film phantoms.

By knowing the maximum imaging depth, it is possible to determine the correspondence between pixels and µm in depth. Due to the symmetry of the Fourier Transform around 0, only half of the cameras pixels along the horizontal direction can contribute

$$1\,\text{px} \mathrel{\widehat{=}} \frac{z_{max}}{\frac{N}{2}} = \frac{z_{max}}{1024} \tag{3.6}$$

Considering the coating of the tear film phantoms 1 pixel corresponds to 0.6 µm and in vacuum to 1.0 µm, respectively. Nevertheless, this is just the image resolution in axial direction based on the sampling. The actual resolution along the longitudinal axis will be limited by the physical axial resolution as discussed in the following chapter.

3.3.2 Axial resolution

The axial resolution depends only on the properties of the light source and is independent of the transversal resolution. It is defined by the coherence length of the light source which is inversely proportional to the spectral bandwidth of the used light source. This is due to the Wiener-Chintschin-Theorem stating that the temporal autocorrelation function of the light field is linked to the spectral power density by Fourier transformation.
In the interferometer, the beam travels to the sample and back, i.e. twice the sample arm length (see figure 3.4). Thus, the axial resolution δz is given by half the coherence length which is inversely proportional to the bandwidth of the light source, and assuming a Gaussian envelope of the spectrum, it is given by

$$\delta z = \frac{l_c}{2} = \frac{2\,ln(2)}{\pi} \frac{\lambda_0^2}{\Delta\lambda} \tag{3.7}$$

where l_c is the coherence length, λ_0 is the central wavelength of the spectrum and $\Delta\lambda$ is its spectral bandwidth ([14], page 26).

In the final setting of the Ti-Sa-Laser the central wavelength and the spectral bandwidth

are (according to figure 3.2) $\lambda_0 = 740.5\,\text{nm}$ and $\Delta\lambda = 136.7\,\text{nm}$, respectively. This leads to an a axial resolution in vacuum of

$$\delta z = \frac{2\,ln(2)}{\pi}\frac{740.5\,\text{nm}^2}{136.7\,\text{nm}} = 1.8\,\mu\text{m}. \tag{3.8}$$

In an medium with refractive index n, the axial resolution changes to

$$\delta z = \frac{1}{n}\frac{2\,ln(2)}{\pi}\frac{\lambda_0^2}{\Delta\lambda}. \tag{3.9}$$

The coatings of the tear film phantoms have a refractive index $n = 1.62$ in the wavelength region of 740 - 840 nm. Therefore the axial resolution improves to $\delta z = 1.1\,\mu\text{m}$.

3.3.3 Lateral resolution

The lateral resolution is independent of the bandwidth of the light source and determined by the focusing optics and the camera chip sampling.
The lateral resolution is diffraction limited by optical contraints of the imaging optics in front of the sample. In this setup, these are given by the beam diameter after the collimator $D_{coll} = 6.9\,\text{mm}$ (as calculatd in appendix B.1.2) and the focal length of the cylindrical lens CL1 with $f_{CL1} = 75\,\text{mm}$. The spherical lenses L1 and L2 are just relaying the focused line onto the sample without additional magnification.

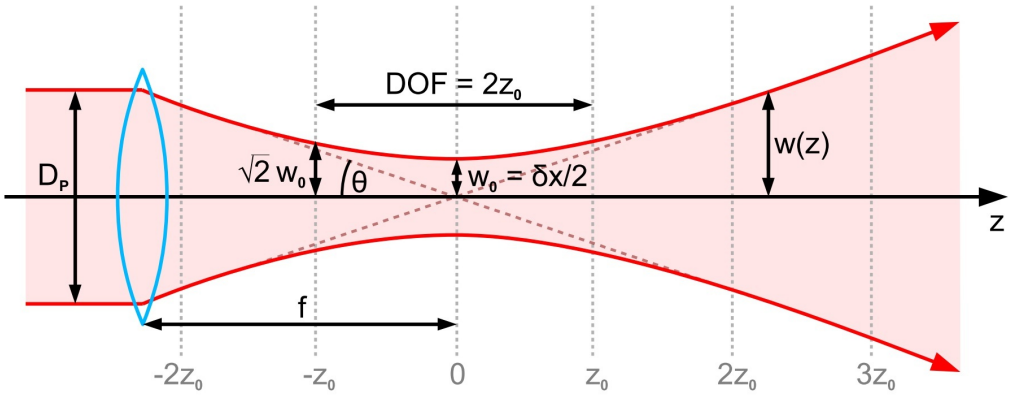

Figure 3.6: Lateral resolution and DOF defined by the focused Gaussian beam ([20], page 53).

The beam diameter of a focused Gaussian beam (as shown in figure 3.6) is given by

$$\delta x = 2\,\omega_0 = \frac{2\,\lambda_0}{\pi\,\theta} = \frac{2\,\lambda_0}{\pi\,arctan(\frac{D_{coll}}{2\,f_{CL1}})} = \frac{2\,\cdot\,740.5\,\text{nm}}{\pi\,arctan(\frac{6.9\,\text{mm}}{2\,\cdot\,75\,\text{mm}})} = 10.3\,\mu\text{m}, \tag{3.10}$$

where λ_0 is the central wavelenght of the light source, $2\,\omega_0$ is the diameter of the focused beam waist, θ the angle of divergence, $D_{coll} = D_P$ the diameter of the incident collimated

beam (as calculatd in appendix B.1.2) and f_{CL1} the focal length of the cylindrical lens CL1.

Additionally to the optical constraints, the lateral resolution is affected by the sampling of the camera chip as well.
Along the horizontal direction the signal is spectrally resolved. In order to reduce the blurriness of the detected spectrum, the following aspect needs to be taken into account. If the diffraction grating is replaced by a mirror under the corresponding angle, the size of the detected spot should not exceed one pixel. Based on that condition, the maximum resolvable spot size in the horizontal direction in the sample plane ($\Delta x_{horizontal}$) is calculated by

$$\Delta x_{horizontal} = pixel\,pitch \cdot \frac{f_{L3}}{f_{L4}} = 5.5\,\mu\text{m} \cdot \frac{75\,\text{mm}}{30\,\text{mm}} = 13.8\,\mu\text{m} \tag{3.11}$$

Thus, the transversal resolution in the horizontal plane (i.e. perpenticular to the line) is limited by the sampling of the camera chip.

Along the vertical direction the line is detected by the camera chip. The minimum resolveable distance between two points in the sample plane is limited by the sampling of the camera chip. According to the Nyquist criterion, at least two pixels are necessary to intentify a detected point as such. Hence, the minimum resolvable distance along the line in the sample plane $\Delta x_{vertical}$ is calculated by

$$\Delta x_{vertical} = 2 \cdot pixelsize \cdot \frac{f_{L3}}{f_{L4}} = 2 \cdot \Delta x_{horizontal} = 2 \cdot 13.75\,\mu\text{m} = 27.5\,\mu\text{m} \tag{3.12}$$

3.3.4 Depth of focus

Just as the lateral resolution, the depth of focus (DOF) is depending on the numerical aperture (NA) of the imaging optics. The DOF is defined as two times the Raleighlength z_R, which describes the distance from the waist at which the focused Gaussian beam widens to $\sqrt{2}w_0$ (as shown in figure 3.6).

$$DOF = 2\,z_R = 2\frac{w_0^2\,\pi}{\lambda_0} = \frac{2 \cdot \lambda_0 \cdot n}{\text{NA}^2}, \tag{3.13}$$

which depends on the refractive index of the sample n and the NA of the imaging optics ([21], page 28).
Because w_0 is proportional to $\frac{\lambda_0}{\text{NA}}$ (this yields DOF proportional to $\frac{\lambda}{\text{NA}^2}$), the DOF is coupled with the lateral resolution via the NA of the imaging optics in such a way, that the better the DOF the worse is the lateral resolution and vice versa. This correlation is illustrated in figure 3.7.

The DOF of the system is given by

$$DOF = 2\frac{w_0^2\,\pi}{\lambda_0} = \frac{\delta x^2\,\pi}{2\,\lambda_0} = 225\,\mu\text{m}, \tag{3.14}$$

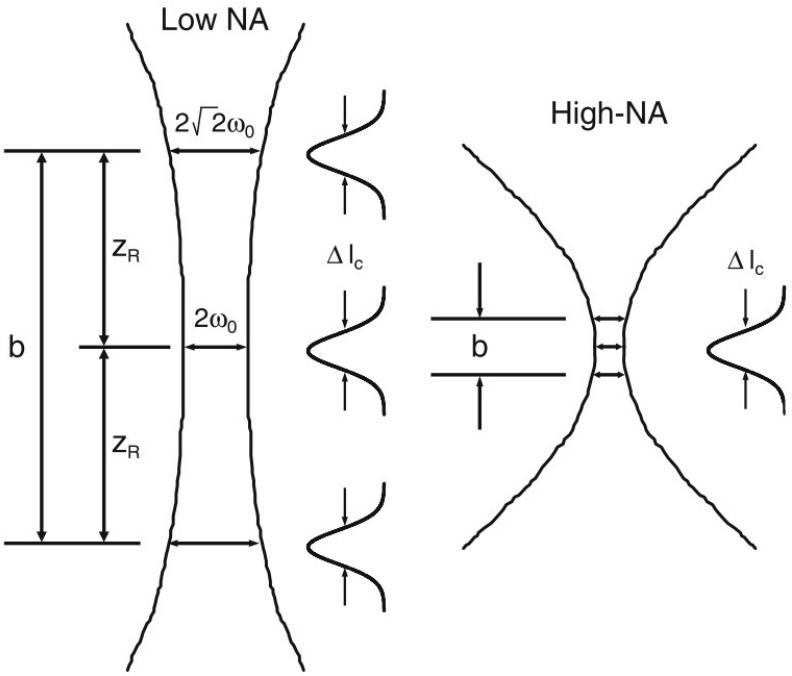

Figure 3.7: Influence of the NA on the lateral resolution and the DOF ([14], page 28)

where δx is the lateral resolution (see equation 3.10) and $\lambda_0 = 740.5$ nm the central wavelength of the Ti-Sa-Laser.

3.3.5 Theoretical line length

After the input collimator the beam is imaged onto the sample without further magnification along the vertical direction. As a consequence, the theoretical length of the illuminated line at the sample is given by the diameter of the collimated beam assuming that the beam is not be cut by the aperture of the lens.
The calculation of the diameter of the collimated Gaussian beam results in a theoretical line length at the sample of 6.9 mm (for detailed calculation see appendix B.1.2).

3.3.6 Maximum power on the eye

The following calculations are based on the ones performed by Fechtig et al. [13] which fulfill the international standard for safety of laser products IEC 60825-1 [22].

The maximum permissible exposure (MPE) for light beams entering the pupil is higher for spatially extended sources compared to a collimated beam. Figure 3.8 shows the ge-

ometry of both situations. In case of line illumination, the pupil of the eye is illuminated by a line focused in the tangential plane, while being collimated in the orthogonal sagittal plane.

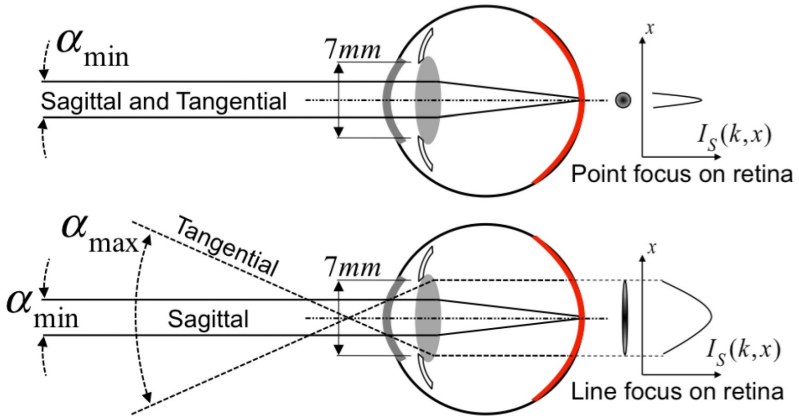

Figure 3.8: Schematic beam geometry for calculating the MPE of the retina in case of point illumination (top) and line illumination (bottom) ([13], page 10).

The MPE for ocular exposure with a static beam is calculated by

$$\text{MPE} = 1.8 \cdot 10^{-3} \cdot C_4 \cdot C_6 \cdot t^{-0.25}\,[\text{W/cm}^2], \tag{3.15}$$

where the factor C_4 depends on the wavelength (λ_C=740.5 nm in case of the final setting of the Ti-Sa-Laser) and is determined by

$$C_4 = 10^{0.002\,(\lambda_C - 700)} = 10^{0.002\,(740.5-700)} = 1.2\,, \tag{3.16}$$

C_6 depends on the angular extent α of the light source and t is the time that the retina is exposed to the radiation. While illuminating the eye with a line, the factor C_6 is calculated by

$$C_6 = \frac{\alpha_{max} - \alpha_{min}}{2 \cdot \alpha_{min}} \tag{3.17}$$

and is proportional to the arithmetic mean of the angles α_{min}=1.5 mrad and α_{max}. If the actual tangential angular subtend $\alpha \geq \alpha_{max}$, then α_{max} is given by α_{max}=100 mrad else C_6 depends on α instead of α_{max}. The underlying geometry of these minimal and maximal angular extents are illustrated in figure 3.8 (bottom).
In this setup, the collimated beam (after the input collimator) has a diameter of 6.9 mm (see appendix B.1.2) which results, along with the imaging optics, in an angular extent of α=92 mrad in front of the pupil. This yields to C_6 = 30.17.

So far, the measurements of the tear film phantoms (see chapter 4.2.1) have been performed by using continuous illumination. In future, for 3-dimensional in vivo measurements it will be necessary to introduce a scanner. The scanning speed will be defined by the intended oversampling that gives the ”residence time” of the line at one position.

While performing the measurements of the tear film phantoms, the maximum possible camera exposure time of 6.5 ms per frame has been necessary due to a low signal to noise ratio caused by back reflections on the interferometer lenses (especially CL2). Hence, in this evaluation of the MPE, the time that the retina is exposed to radiation was considered to be the maximum exposure time of the camera.
This yields to a MPE on the eye of

$$\mathrm{MPE} = 1.8 \cdot 10^{-3} \cdot 1.2 \cdot 33.8 \cdot 6.5^{-0.25} = 40.94\,\mathrm{mW/cm^2} \tag{3.18}$$

Following that, the maximal power illuminating the eye (MPΦ) is determined by multiplying the MPE with the full pupil area of $A_{Pupil} = 0.385\,\mathrm{cm^2}$.

$$\mathrm{MP\Phi} = \mathrm{MPE} \cdot A_{Pupil} = 40.94\,\mathrm{mW/cm^2} \cdot 0.385\,\mathrm{cm^2} = 15.76\,\mathrm{mW} \tag{3.19}$$

3.4 System alignment

The whole optical system (except the dispersion compensation prism pair and the spectrometer) was aligned with the Superlum SLD and the following guidelines were taken into account.

The tilts of the reference and sample mirror were orientated in such a way that the reflected beam is travelling along the same path as the incident beam. This was for example for the reference mirror ensured by placing a pinhole in the centre of the incident collimated beam in the reference arm. The pinhole aperture is minimized and the optical power is measured in the detection arm while the reference mirror is tilted until the power is maximized.

The central position of all lenses (especially the ones in the interferometer) need to be very accurate. For this reason, the lenses were centrally aligned in respect to the incident collimated beam. The first lens inserted into the system and aligned centrally was L3, followed by L2, L1 and CL1 as well as CL2. In order to align the lenses centrally in the first step and their focus positions in the second step, L1, L2 and L3 were mounted in a caged system.

Subsequently, the focal positions of all lenses were precisely aligned starting with CL1 and followed by CL2, L1, L2 and L3. For the accurate alignment of the focal and the central positions the beam profiler (WinCamD UCD12, DataRay Inc., Redding, CA, USA) was used.

The focus position of the sample mirror was aligned by deflecting the beam in the detection arm between L3 and the diffraction grating and inspecting it through a telescope. The focus of the sample mirror was varied until the signal from the sample arm was observed as sharply as the one from the reference arm.

The dispersion compensation prism pair and the spectrometer were aligned with the Ti-Sa-Laser. The position of the spectrometer lens L4 was optimized by replacing the diffraction grating by a mirror. This mirror was aligned in such a way, that the reflected beam propagates along the same path as the central wavelength would do in case of the diffraction grating. By use of the mirror, all wavelengths are superimposed at the camera chip resulting in a sharply focused vertical line on condition that L4 and the camera chip are placed in their right focal positions. Moreover, the centre of the imaged beam should be the same no matter if with or without L4. These facts were used to align L4 centrally and in the right axial position.

3.5 Data aquisition

3.5.1 Features of the camera

The camera must fulfill the following requirements in order to ensure a high quality of image in future in-vivo measurements:

- The best sample would be a static one, because movements lead to artefacts and in extreme cases to fringe washout. The human eye moves always a little bit causing inaccuracy in the obtained images. In order to minimize these motion artefacts, the camera needs to have a high frame rate and short exposure time.

- The lateral resolution of a single B-scan, in other words how close two neighbouring points of the same layer can be displaced in order to be still distinguishable from each other, is influenced by two aspects. One is the geometrical limitation by the optics in the sampling arm and the other one the limited number of pixels on the camera chip. In order to minimize the influence of the sampling of the camera, the camera chip needs to have a large number of pixels over a fixed length. So far, by use of state of the art cameras, this degradation in resolution can not be avoided (see chapter 3.3.3).

The area camera UI-3360CP-NIR-GL (IDS, Obersulm, Germany) with a resolution of 2048 x 1088 pixel was chosen. Its theoretical maximum framerate is 340 fps along with 10 Bit depth and the maximum bit depth of the sensor is 12 Bit along with 70 fps. The camera chip CMV20000-3E12M1PP from the company CMOSIS is specially designed for applications in the near infrared (NIR) region. Nevertheless, the quantum efficiency decreases with increasing wavelength and at 950 nm it has already dropped to 10 % (see figure 3.9). Therefore, in the selection process of the other optical components, care should be taken that they are very efficient in the near infrared region.

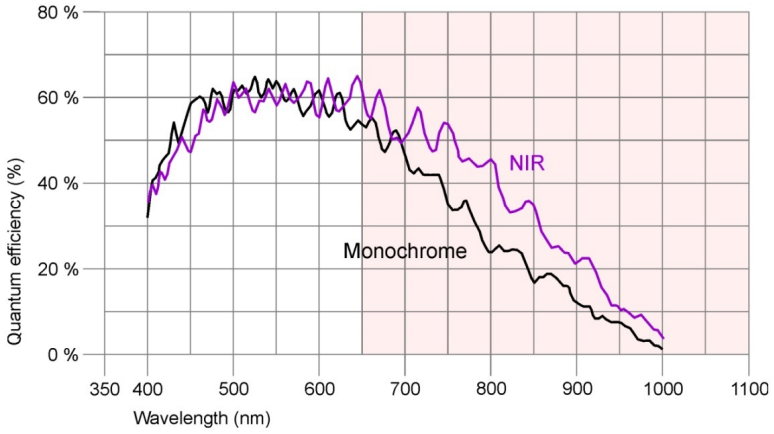

Figure 3.9: The spectral quantum efficiency of the camera chip in use [23].

3.5.2 Acquisition settings and the LabVIEW program

The intensity of the obtained signal depends on the reflectivities of the sample and the reference mirror (see equation 2.6). In order to obtain maximum signals, the maximum possible and allowed light power (in accordance to the laser safety guidelines see chapter 3.3.6) should be applied. The power of the signals obtained from sample and reference arm should be about the same size for a maximum amplitude in the interference pattern which also benefits in keeping the bias signal small. In addition, the whole bit depth of the camera chip should be used without saturating it.

In the recorded spectrum (raw image) the depth information of the reflective layers in the sample is encoded. The depth information is decoded by performing a Fourier transform of the image (see equation 2.8).
The following signal processing steps are necessary before applying the Fourier transform in order to obtain good results from the recorded raw images (see figure 3.10).

The intensity signal is acquired by the spectrometer in λ-space. In order to obtain the sample's depth information it needs to be converted to the linear k-space ($k = 2\pi/\lambda$). Moreover, the intensity values must be equidistant in k-space before applying the Fourier transform to display the depth information correctly. The rescaling is based on the algorithm as used by Doblhoff-Dier [20] (pages 124-131).

Additionally, the resulting OCT signal is improved by subtraction of the reference spectrum. This spectrum is recorded right before measuring the sample and it is obtained by covering only the sample but neither the rest of the sample arm nor the reference arm. The subtraction of the reference spectrum ensures that after the fast Fourier transform (FFT) only sample structures are displayed and that signals arising from reflections at components in the interferometer arms are eliminated. Additionally, this subtraction reduces the bias in the recorded spectrum, thus it minimizes the DC term in the obtained depth profile.

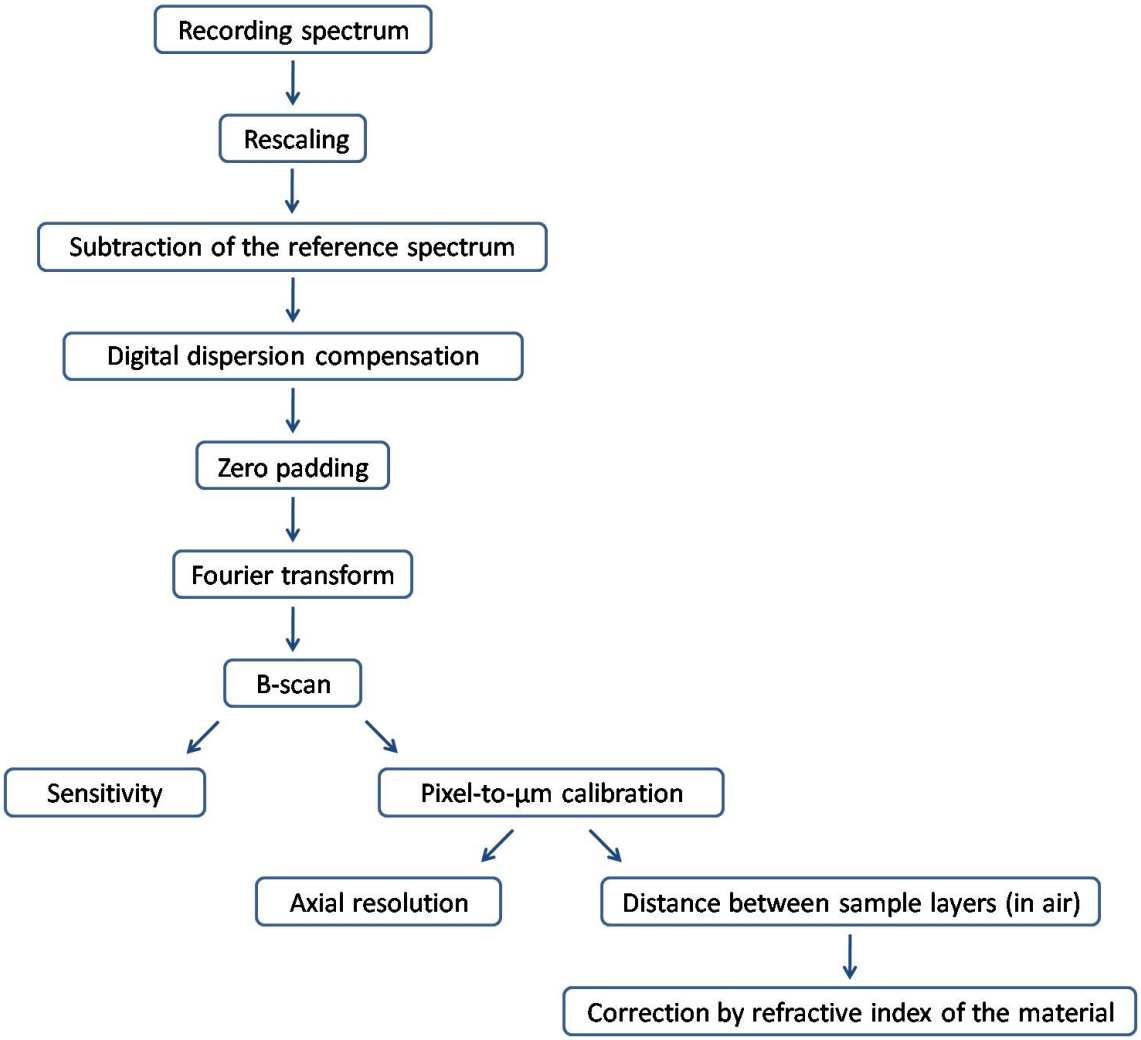

Figure 3.10: Flow chart of the LabVIEW Program

Dispersion compensating prisms were introduced into the reference arm and finely adjusted in order to compensate dispersion caused by the optics in the sample arm. This optically compensation is not perfect and difficult to align, especially due to the large bandwidth of the light source. However, the compensation can be improved by applying a digital dispersion compensation algorithm developed by Wojtkowski et al. [24]:

$$\phi(k)' = \phi(k_0) - a_2(k - k_0)^2 - a_3(k - k_0)^3, \tag{3.20}$$

where two phase correction terms are added to the original phase $\phi(k_0)$ which is replaced by the compensated phase $\phi(k)'$. The factors a_2 and a_3 of the phase correction terms are manually varied. For example in case of imaging the sample mirror, choosing good correction factors improves the peak height of the cross-correlation term as well as ensures that the FWHM of the same is small and constant over the whole depth range.

Zero Padding is an elegant method of interpolating the Fourier transformed signal. In the measurements performed in chapter 4 the width of the detector along the spectral dispersive dimension was enlarged from $2^{11} = 2048$ (number of pixels of the camera chip) to $2^{14} = 16384$ by adding zeros. This enhanced the spectral sampling of the detector. Hence the locations of the reflective layers in the depth profile can be extrapolated with higher accuracy as long as they are far enough apart from each other (at least more than the axial resolution).

After these post-processing steps the final B-scans (2D-tomograms) are displayed, for examples see figures 4.5 and 4.8. The B-scan displays only the amplitude part of the image, which contains the information about the reflective layers of the sample. The phase information of the image may be used as well, e.g. in Doppler OCT for calculation the velocity of a moving sample, but is neglected in this thesis.

Based on this B-scan several parameters can be calculated, e.g. the sensitivity as well as the axial resolution and axial distances between reflecting layers in the samples (see figure 3.10).
The sensitivity was calculated via the signal-to-noise-ratio as explained in chapter 4.1.2.
Furthermore, for measuring lengths in depth a calibration needed to be performed first. Therefore, the conversion factor between a distance in µm along the axial direction in the interferometer and the same distance measured in pixels between the cross-correlation term and the DC-term needs to be evaluated. This is done manually by moving the stage of the reference mirror in small defined steps while measuring the shift (in pixel) of the cross-correlation peak in the depth scan.
After this pixel-to-µm correlation is known the axial resolution is determined by the FWHM of the Fourier transformed terms (see chapter 4.1.3). Additionally, based on this calibration, distances between reflecting layers of the sample are evaluated (see chapter 4.2). The calibration was performed with the sample mirror which was surrounded by air. For measuring axial distances between layers of a sample the pixel-to-µm correlation needs to be corrected by the refractive index of the material.

Chapter 4

Results and Discussion

4.1 System characterization

4.1.1 Wavelength dependency of the components

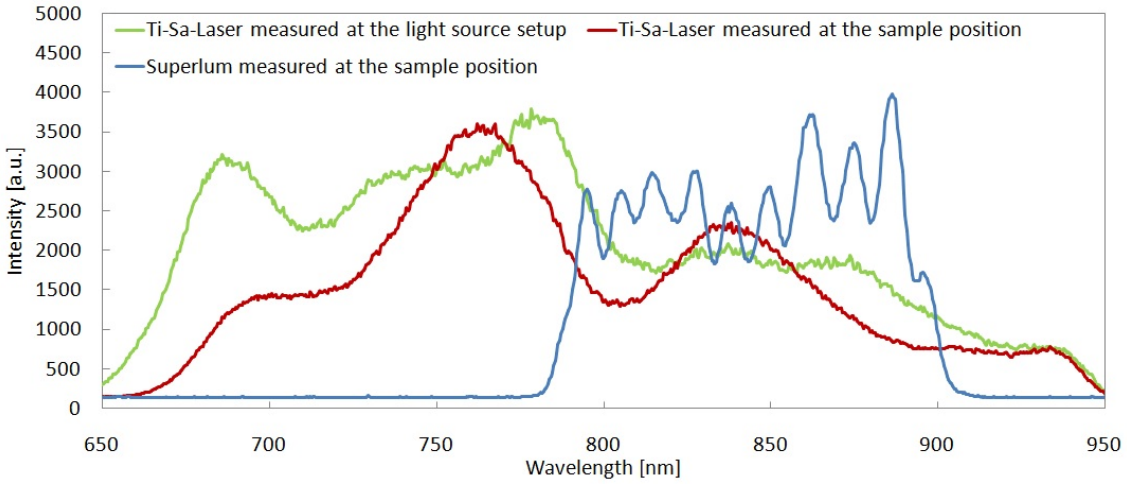

Figure 4.1: Spectra of the Ti-Sa-Laser and the Superlum SLD measured at the sample position as well as measured spectrum of the Ti-Sa-Laser at its output. The spectra were measured with a high-resolution spectrometer (HR2000CG-UV-NIR, Ocean Optics, Dunedin, Florida, USA).

As sown in the figure 4.1, the spectrum of the Ti-Sa-Laser changes between its optical table, where the laser itself is located, and the sample position in the OCT system. This may be caused by the single mode fiber (SM750, fibercore, Southampton, U.K.) transmitting the signal from the optical table of the Ti-Sa-Laser to the OCT setup over 20 m length. Its operating wavelength range is 780 - 830 nm and the fiber changes the spectrum shape below its cut off wavelength of 750 nm. Additionally, the spectrum is attenuated by

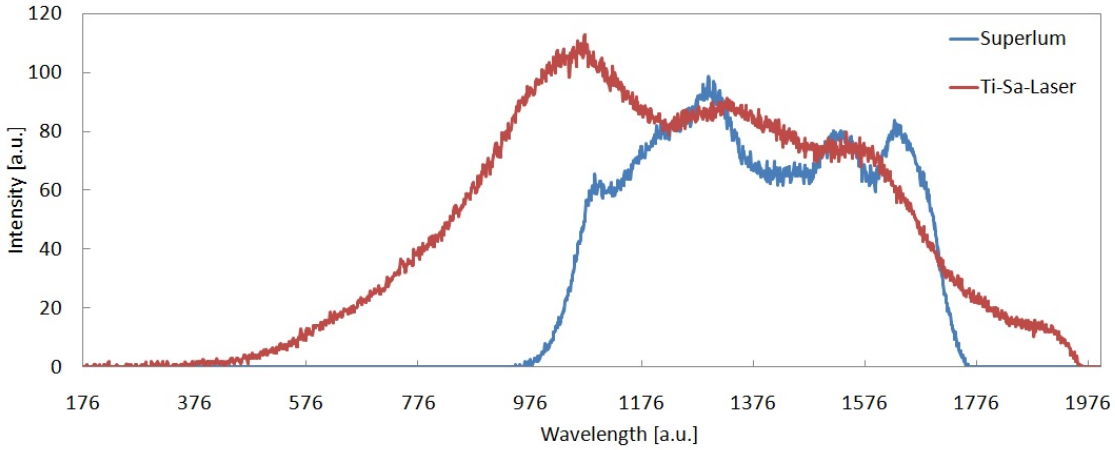

Figure 4.2: By the OCT setup spectrometer measured spectra of the Ti-Sa-Laser and the Superlum SLD.

the beam splitter which reflectance decreases from 50% at 700 nm to 5% around 620 nm.

Furthermore, the shape of the spectrum of the Ti-Sa-Laser changes between the sample position and the camera chip (see figure 4.1 and 4.2). This is caused by the diffraction grating which is blazed at 840 nm. Its transmission efficiency is the highest around this wavelength and decreasing for shorter and longer wavelengths. The transmission efficiency is ca 87% at 830 nm and decreasing to ca 63% at 700 nm. Moreover, the spectrum is influenced by the detection itself using a camera based on a CMOS sensor. The quantum efficiency of the camera chip decreases with increasing wavelength from 35% at 840 nm to 10% at 950 nm (see figure 3.9). No influence on the spectrum is expected by the coating of the lenses, because their transmission is almost constant in the range of 650 - 1050 nm. Mainly due to the diffraction grating and the camera chip, the incoming light is least affected around 830 nm and strongly attenuated for shorter and longer wavelengths.

Another rather small effect could have the fact that the system (concerning all imaging optics except the dispersion compensation prism pair, the diffraction grating and the spectrometer lens L4) was aligned with the Superlum SLD light source. Hence, the alignment of the lenses (except L4) is optimized for wavelengths close to the central wavelength of the Superlum SLD $\lambda_0 = 840\,\text{nm}$.

Considering all mentioned effects depending on the wavelength, as well as the spectrum detected by the setup's spectrometer (see figure 4.2), it can be assumed that the detected spectrum of the Ti-Sa-Laser has another shape, thus an other central wavelength λ_C and bandwidth $\Delta\lambda$, than the initial one. Comparing the initial spectra, the bandwidth $\Delta\lambda$ of the Ti-Sa-Laser is by a factor of 1.37 bigger than the one obtained with the Superlum SLD, while in case of the detected spectra the factor is only 1.25. This shows, a significant reduction of the bandwidth of the Ti-Sa-Laser by the components of the setup.

The proper interpretation of the obtained data can be improved by knowing λ_0 and $\Delta\lambda$ of the actual detected Ti-Sa-Laser spectrum. For that reason a calibration of the setup spectrometer would be of great benefit. Unfortunately, no adequate light source was available for this purpose.
Comparing the spectra obtained from the Superlum SLD in different depth positions of the interferometer (see figure 4.1 and 4.2), motivates the assumption that the spectrum shape (i.e. λ_C, $\Delta\lambda$) of the Superlum SLD is not changed by the previously discussed effects. Hence, the Superlum SLD can be used as a reference for estimating the properties of the detected spectrum of the Ti-Sa-Laser. This yields, to an estimated central wavelength $\lambda_0 \approx 820\,\text{nm}$ and bandwidth $\Delta\lambda \approx 125\,\text{nm}$ of the detected Ti-Sa-Laser spectrum.

4.1.2 Maximum sensitivity and sensitivity roll off

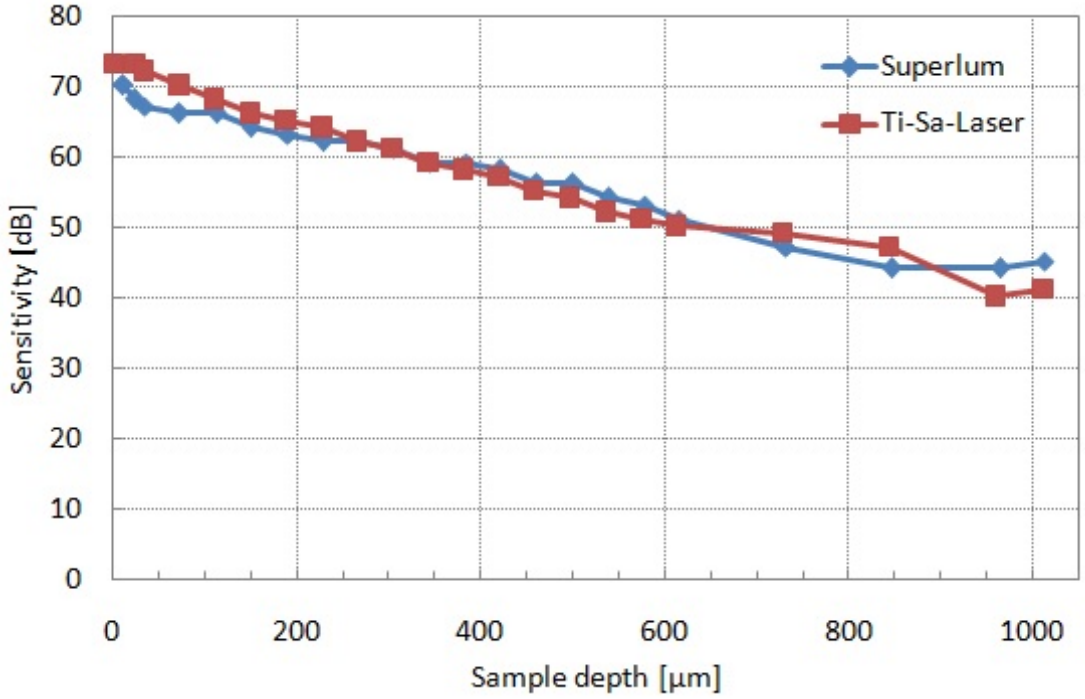

Figure 4.3: Axial sensitivity roll off measured with the Ti-Sa-Laser as well as the Superlum SLD light source.

The sensitivity is defined by the ratio of the signal and the noise. If they are equal the sensitivity is 1 ([14], page 229). For a shot noise limited system, the sensitivity is given by

$$Sensitivity|(dB) = -10\,log\left(\frac{\eta\,P_0}{h\,\nu\,f_A}\right), \tag{4.1}$$

where η is the detector sensitivity, P_0 the optical power incident on the sample, $h\nu$ the single photon energy and f_A is the A-line rate.

In the case of LF-SD-OCT this formula changes to

$$Sensitivity|(dB) = -10\,log\left(\frac{\eta_{Cam}\,P_0\,\Delta t}{h\,\nu\,M}\right), \tag{4.2}$$

where η_{Cam} is the quantum efficiency of the camera chip, Δt is the total B-Scan acquisition time (i.e. the integration time of the camera) and M are the number of pixels illuminated along the line (i.e. the FWHM of the line length given in pixels). This yields a shot noise limited sensitivity of 83.6 dB for the Superlum SLD and 88.0 dB in case of the Ti-Sa-Laser (see table 4.1).

Table 4.1: Shot noise limited sensitivity and parameters used for calculation

	η_{Cam}	P_0 [µW]	Δt [ms]	M	Sensitivity [dB]
Ti-Sa-Laser	0.52	27.6	6.52	215	88.0
Superlum SLD	0.53	13.1	6.52	215	83.6

The experimental sensitivity was obtained by measuring the minimum detectable reflectivity as described by Leitgeb et al. [16]. In front of the sample mirror a NDF with OD = 1.3 was placed. Then the reference arm signal was attenuated by the variable NDF in the reference arm such that the interferometer signal was close to the saturation value of the camera. This was done in order to attain maximal possible modulation amplitude on the camera chip leading to an optimal SNR. The sensitivity was calculated by

$$Sensitivity|(dB) = -10 \cdot log\left(\frac{Signal\ peak\ after\ DFT^{\,2}}{Ambient\ noise\ rms^{\,2}}\right) + 20 \cdot OD_{NDF}. \tag{4.3}$$

The maximum sensitivity obtained by a signal peak close to the DC peak was 70 dB for the Superlum SLD and 73 dB in case of the Ti-Sa-Laser. Addtionally, a sensitivity roll off in depth was measured by moving the reference mirror along the axial direction (see figure 4.3). In a depth of 2/3 of the maximum imaging depth z_{max} the sensitivity decreased to 51 dB in case of the Superlum SLD and to 50 dB for the Ti-Sa-Laser.

Moreover, the intensity along the line is decreasing from the maximum in the centre to the line ends and so does the sensitivity as well. A vertical intensity profile along the line is shown in figure 4.4. The asymmetric shape of the intensity profile along the line may be caused by the mounting of the prism pair. The height of the prism pair is 10 mm and thus rather small compared to the incident beam diameter of 6.9 mm. Hence, some part of the beam diameter might be blocked by the mounting.

It is more important to improve the maximum sensitivity and the sensitivity roll off in axial direction before the sensitivity roll off along the line is discussed in detail, that is why this chapter focus on the former.
In the following paragraphs, the differences between the calculated and the measured sensitivities (14 dB in case of the Ti-Sa-Laser and 13.6 dB for Superlum SLD) as well as the

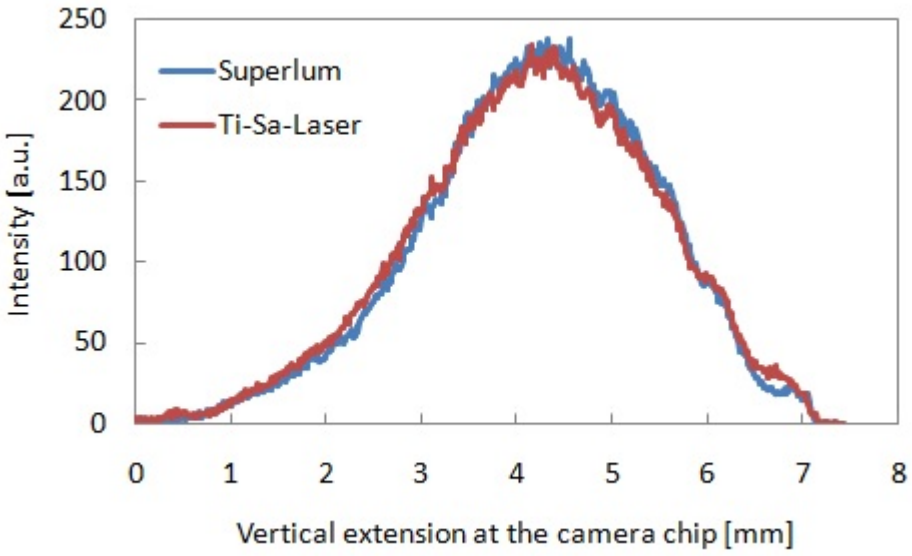

Figure 4.4: Vertical intensity profile along the line while imaging a mirror with the Ti-Sa-Laser as well as the Superlum SLD light source. The vertical extension axis was converted from pixel index to the lateral dimension in mm based on the factor which was obtained by measuring a reticle with known line spacing (see chapter 4.1.4).

sensitivity roll off in depth are discussed.

The low sensitivity is mainly caused by the back reflections of all interferometer lenses, especially by the cylindrical lens CL_2. The back reflections are present in all measurements and overlap with the signal of interest at the camera chip. Consequently, they reduce the available bit depth for the signal of interest and thus the sensitivity. If the back reflections on the camera chip could be eliminated, the whole bit depth could be used by the interference signal. Subsequently, the power on the sample could be increased without saturating the camera. Thus, leading to a significant improve of sensitivity.
All applied powers on the different samples while performing the measurements of the results chapter were far below the maximum permissible power on the eye (15.76 mW, calculated in chapter 3.3.6). For the measurements with the Ti-Sa-Laser, a very small power of 254 nW was applied on the sample mirror and 1.27 µW on the glass plate. In case of the tear film phantoms, optical powers in the range of 300-400 nW were used. These low values were chosen due to the strong back reflections which had to be minimized.
Obviously, by eliminating the back reflections, the sensitivity could easily be improved, theoretically even by

$$10\,log\left(\frac{MP\Phi}{P_{Sample}}\right) \approx 40\ -\ 47\,dB \tag{4.4}$$

However, in this configuration the camera would probably be totally saturated. It is more

realistic, that by applying an appropriate power the improvement will be in the range of 25 - 30 dB.

Another issue of the setup are changes on the imaged spectrum induced by wavelength dependent transmission of the components, leading to attenuation of parts of the spectrum (as already discussed in chapter 4.1.1). The shot noise limited sensitivity (equation 4.1) was calculated for the initial spectrum of the Ti-Sa-Laser ($\lambda_0 = 740\,\text{nm}$). However, the detected spectrum differs from the initial one in terms of shape and central wavelength $\lambda_0 = 820\,\text{nm}$.
With increasing wavelength, the quantum efficiency of the camera chip is decreasing. This yields a shot noise limited sensitivity of 87.5 dB in case of $\lambda_0 = 820\,\text{nm}$, i.e. a loss of -0.5 dB compared to the calculated sensitivity at $\lambda_0 = 740\,\text{nm}$. This is an acceptable decrease in sensitivity and obviously the camera chip is designed for the NIR.

Whether the sample position is exact in focus or not, has an influence on the sensitivity as well. The sensitivity is determined by the SNR, and in shot noise-limited operation mode along with absence of scattering it is given by ([14], page 110)

$$(SNR)_0 = \frac{4 p_b \eta P_S}{h\nu B_W} \left(\frac{w_0}{f}\right)^2, \tag{4.5}$$

where f is the focal length of the imaging optics in front of the sample and w_0 is the beam waist radius in focus. The ratio of both, as given in equation 4.5, is equal to the NA of the sample objective in the paraxial approximation. Therefore, the SNR can be rewritten as

$$(SNR)_0 = \frac{4 p_b \eta P_S}{h\nu B_W}\,\text{NA}^2 \propto \text{NA}^2. \tag{4.6}$$

Thus the sensitivity is proportional to the square of the NA of the imaging optics in front of the sample. Within the DOF, the beam radius widens from w_0 at the focal position to the end of DOF by the factor $\sqrt{2}$, leading to an equivalent optical system with an NA reduced by the same amount. In accordance to equation 4.6, this leads to a decrease in sensitivity by -3 dB at the edge of the DOF.

During the sensitivity roll off measurements, the detected spectrum was not modulated over its whole spectral range. This may be caused by a little tilt of the sample stage in relation to the optical axis.
For the sensitivity roll off measurement, a NDF is added in the sample arm. This additional glass plate is changing the axial focus position at the sample which need to be adapted to the new focus. As a consequence of the little tilt of the sample stage, by changing its position, the beams from the sample and reference arm are not collinear in the detection arm. At the camera chip, this leads to an offset between the beams from the two interferometer arms. Hence, the two spectra are only partially overlapping that is why the modulated spectral range as well as the sensitivity are limited.
By moving the reference mirror along the axial direction, the offset increases leading to a

larger sensitivity roll off. This issue might be solved by optimizing the adjustment of both arms of the interferometer over a longer depth range and defining a calibration curve for the whole depth range.

Moreover, a high dispersion mismatch between the two interferometer arms may be the main reason for the large sensitivity roll off in depth.
The optical dispersion compensation (prism pair) was optimized for the sample mirror without the additional NDF in the sample arm. For measuring the sensitivity roll off, a NDF was added in the sample arm. Thereby, additional dispersion was induced, but the prism pair was not readjusted to not alter the setup for further measurements on tear film phantoms. Subsequently, during the data analysis, a digital dispersion compensation algorithm was applied and performed for each position in depth. Nevertheless, the dispersion mismatch could not be fully compensated by this algorithm. Because of that, the cross correlation peak of the Fourier transformed spectrum is broadened. This reduces not only the SNR along with the sensitivity but also the axial resolution.
In general, the dispersion compensation is difficult to adjust for broad bandwidth light sources.

4.1.3 Measured axial resolution

The axial resolution is defined by the FWHM of the field autocorrelation of the light source (see chapter 3.3.2). The envelope of the field correlation equals the Fourier transform of the power spectrum. Hence, the axial resolution is measured as the FWHM of the various terms of the field correlation function, i.e. the DC term, the auto-correlation as well as the cross-correlation terms (see equations 2.6 and 3.7).
In the case of ideal imaging and infinite fine sampling of the acquisition the calculated theoretical value equals the measured FWHM of the DC term as well as of the single auto-correlation and cross-correlation terms. Real-life conditions cause deviations between these values and will be discussed in the following paragraphs (see overview in table 4.2).

The measured axial resolution discussed in this chapter was obtained by imaging a sample mirror. This sample consists of only one reflecting layer, therefore the Fourier transformed signal contains only the DC term and one cross-correlation term. The FWHM of the cross-correlation term is the actual axial resolution of the system while imaging a reflective surface surrounded by air. An actual axial resolution of 3.7 µm and 4.5 µm was achieved with the Ti-Sa-Laser and the Superlum SLD, respectively.

The spectrum of the Ti-Sa-Laser detected by the camera had a smaller bandwidth (approximately only 125 nm, see chapter 4.1.1) than the one measured at the Laser output. This yields a theoretical axial resolution of 2.4 µm.
Additionally, the axial resolution is limited by the sampling of the spectrometer which

Table 4.2: Comparison of the theoretical calculated axial resolution with the measured on and taking into account the step size of the sampling by the camera chip. All values are given in μm. The measured axial resolution is obtained by measuring a mirror in air.

Theoretical resolution (air) [μm]		
	Initial spectrum	Detected spectrum
Ti-Sa-Laser	1.8	2.4
Superlum SLD	3.1	3.1
Measured resolution (air) [μm]		
	Cross-correlation peak	DC peak
Ti-Sa-Laser	(3.7 ± 1.0)	(3.0 ± 1.0)
Superlum SLD	(4.5 ± 1.0)	(3.7 ± 1.0)

is in this setup the spectral step size defined by the camera chip and was measured as 1.0 μm/Pixel in air.

Considering both influences, this can lead to a broadening of the axial resolution. Hence, the measured axial resolution values are expected within a range, e.g. 1.4 - 3.4 μm in case of the used Ti-Sa-Laser. The measured FWHM of the DC terms agree with this expectation, but the measured FWHM of the cross-correlation terms are slightly out of range (by 0.3 μm and 0.4 μm measured with the Ti-Sa-Laser and the Superlum SLD light source, respectively).
The reasons therefore are most probably:

- The influence of the dispersion mismatch between the reference and sample arm which could be further improved. The measured cross-correlation axial resolution differs slightly more from the theoretical value by using the Superlum SLD than in case of the Ti-Sa-Laser. This may be due to the fact that the prism pair was aligned with the Ti-Sa-Laser.
  Taking into account the large bandwidth, one could envisage improving the digital dispersion correction by using higher order terms of the dispersion function and automating the algorithm.

- The equation used to calculate the theoretical axial resolution assumes a Gaussian envelope of the spectrum. Considering the measured spectra, this assumption applies only approximately. An option to overcome this issue would be to use additional windowing during the post processing before the FFT is calculated.

- As the sampling of the camera chip is rather low compared to the measured axial resolution, the values are still within a confidence interval of twice the error margin. Note that the next sampling point would lie at 4.4 μm and 5.1 μm for the Ti-Sa-Laser and the Superlum SLD light source, respectively. The step size could be improved

by designing the spectrometer to the effective bandwidth of the light source and increasing the number of the pixels on the camera chip.

The measured axial resolution could be further enhanced by adjusting the Ti-Sa-Laser to a higher central wavelength while maintaining or even enlarging the bandwidth.
Normally the resolution improves by increasing the spectral bandwidth and decreasing the central wavelength of the light source in use.
In respect to the wavelength dependent transmission efficiency of the setup discussed in this thesis (see chapter 4.1.1), the detected spectral bandwidth could be enlarged by adjusting the Ti-Sa -Laser to a higher central wavelength close to 800 nm while retaining the same bandwidth. This is due to the fact, that all components where chosen for the initially planned light source, the Ti-Sa-Laser with a central wavelength of 800 nm.

4.1.4 Measured illumination line length

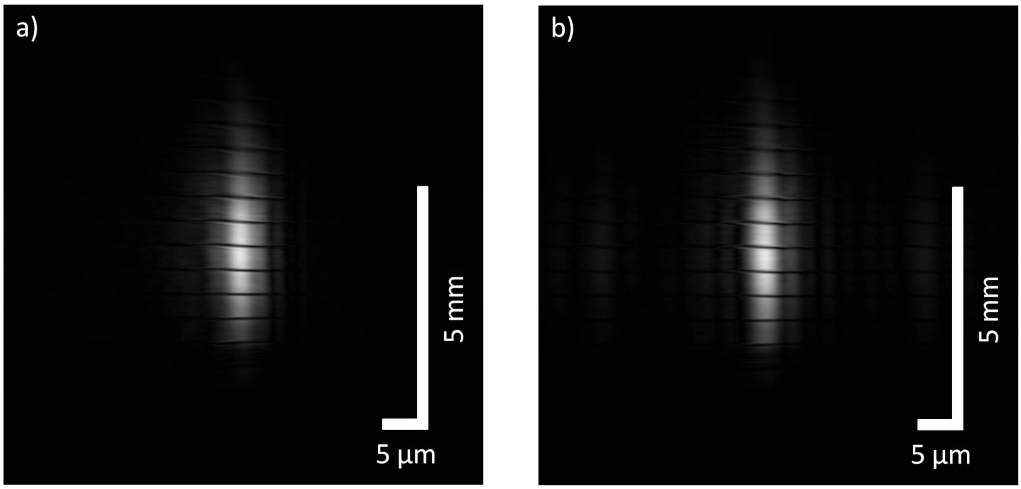

Figure 4.5: 2D tomograms of a reticle obtained with (a) the Ti-Sa-Laser and (b) the Superlum SLD light source.

A reticle with a grid with 500 µm spacing between the lines and a line thickness of approximately 20 µm was measured (reticle No. 7 from the package 39-098, Edmund Optics GmbH, Karlsruhe, Deutschland). Along the line illumination (vertical direction) the lines of the grid are quite sharply imaged. This suggests that the vertical lateral resolution is at least in the magnitude of 20 µm in good agreement with the theory of around 13 µm (sampling of CMOS).

The measurements of the glass plate including a grid was performed in order to evaluate the length of the line illuminating the sample. The line length was measured at the edges where the intensity had dropped to 10% of the maximum line intensity. The measured line lengths were found to be 5.59 mm and 5.17 mm for the Ti-Sa-Laser and the

Superlum SLD light source, respectively. These measures were used to calibrate the lateral scale along the line.

As the maximum imaging depth z_{max} of the system was smaller than the thickness of the reticle, only the front surface reflex of the sample is visible in the tomogram.

4.2 Measurement and characterization of samples

4.2.1 Evaluation of the thickness of tear film phantoms

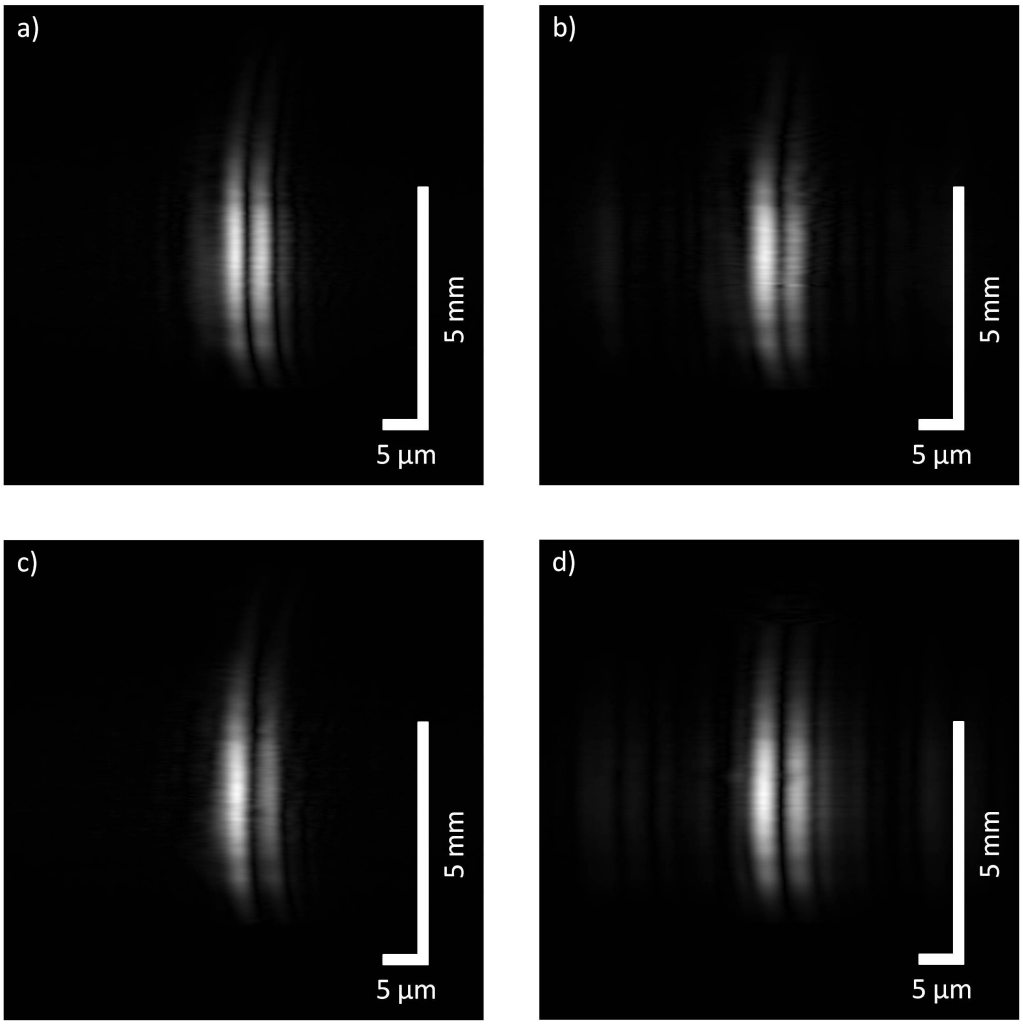

Figure 4.6: 2D tomograms of the Tear-Film-Phantoms. One phantom with the reference value 3.26 µm measured with (a) Ti-Sa-Laser and (b) Superlum SLD. Another phantom with the reference value 3.67 µm imaged with (c) Ti-Sa-Laser and (d) Superlum SLD.

The phantoms were produced by a photolithography technique used for semiconductor devices fabrication. In this process a layer of photoresist lacquer (AZ6632 Microchemicals GmbH, Ulm, Germany) was applied on a Silicon substrate (Si). In the following the measured thicknesses are compared with reference values obtained with white light interferometry (F20-UVX-thinfilm analyzer, Filmetrics Inc., San Diego, CA, USA).

The tomograms in figure 4.6 show that the tear film phantoms with thicknesses in the range of 3.26 - 4.81 µm can be resolved with the discussed setup.

Moreover, figure 4.6 shows the decrease in intensity from the centre to the edges along the line illumination. Besides, the slight curvature of the line in the displayed tomograms is most likely to be due to some field curvature and distortion. These aberrations are inherent in optical systems.

In most tomograms obtained with the Ti-Sa-Laser the cross-correlation peaks have a smaller FWHM and the tomograms appear sharper than the ones imaged with the Superlum SLD light source. This is a consequence of the higher axial resolution obtained for the Ti-Sa-Laser and shown by the tomograms (a) and (b) in figure 4.6 obtained with the Ti-Sa-Laser and the Superlum SLD, respectively.
However, by measuring another wafer with the Ti-Sa-Laser, the tomogram (c) appears a little bit blurred and the cross-correlation peak has a bigger FWHM than the one in tomogram (a), this is probably caused by some uncompensated dispersion. Moreover, in the tomogram (c), the intensity of the reflex of the front surface is stronger than the one of the back surface. This is probably caused by the focus being placed above the front surface of the phantom.

The thickness of the tear film phantoms was evaluated by analysing the depth profile in the point of the maximum intensity along the line. Based on the obtained depth profiles, the thickness was evaluated by precisely computing the peak position for both, front and back surface of the phantom, and taking the difference from both measurements (see figure 4.7). This procedure was performed for three different points on the surface of each tear film phantom. Subsequently, the measured thicknesses of these points were averaged and compared with the reference values obtained with white light interferometry (see table 4.3).

Comparing both imaging modalities, LF-SD-OCT vs. white light interferometry, the highest deviation can be found at sample No. 2. There, the measured value with OCT (Ti-Sa-Laser) is around 0.5 microns lower than with the reference method. This is acceptable as the axial step size in the tear film phantom is 0.62 µm considering a refractive index of 1.61. Additionally, the roughness of the tear film phantom surface as well as slight tilt of the sample itself can result in these kind of differences. However, it is obvious that the proposed LF-SD-OCT setup is able to resolve the thin film layer which show are comparable thickness to the pre corneal tear film.

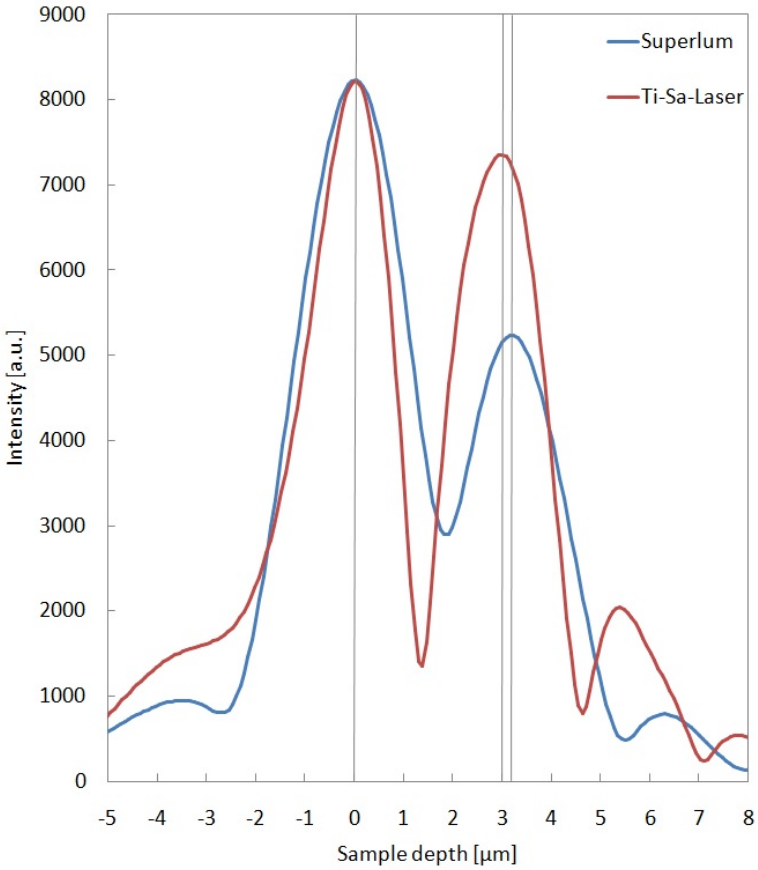

Figure 4.7: Depth profils of the tear film phantom with the reference value of 4.00µm obtained with the Ti-Sa-Laser and the Superlum SLD.

Table 4.3: The results obtained by measuring the thickness of the tear film phantoms with the Ti-Sa-Laser as well as the Superlum SLD light source in comparison with the reference values from white light interferometry. Every phantom was measured with each light source in three different locations and the maximum variation is given in [%].

Ti-Sa-Laser mean value [µm]	Ti-Sa-Laser max. variation [%]	Superlum SLD mean value [µm]	Superlum SLD max. variation [%]	Reference [µm]
(4.74 ± 0.62)	1.2	(4.85 ± 0.62)	1.3	4.81
(3.80 ± 0.62)	0.9	(4.30 ± 0.62)	0.4	4.31
(4.00 ± 0.62)	1.0	(4.12 ± 0.62)	1.9	4.00
(3.80 ± 0.62)	1.0	(3.71 ± 0.62)	2.2	3.67
(3.02 ± 0.62)	3.9	(3.23 ± 0.62)	0.9	3.26

4.2.2 Evaluation of the system by measuring a cover glass plate

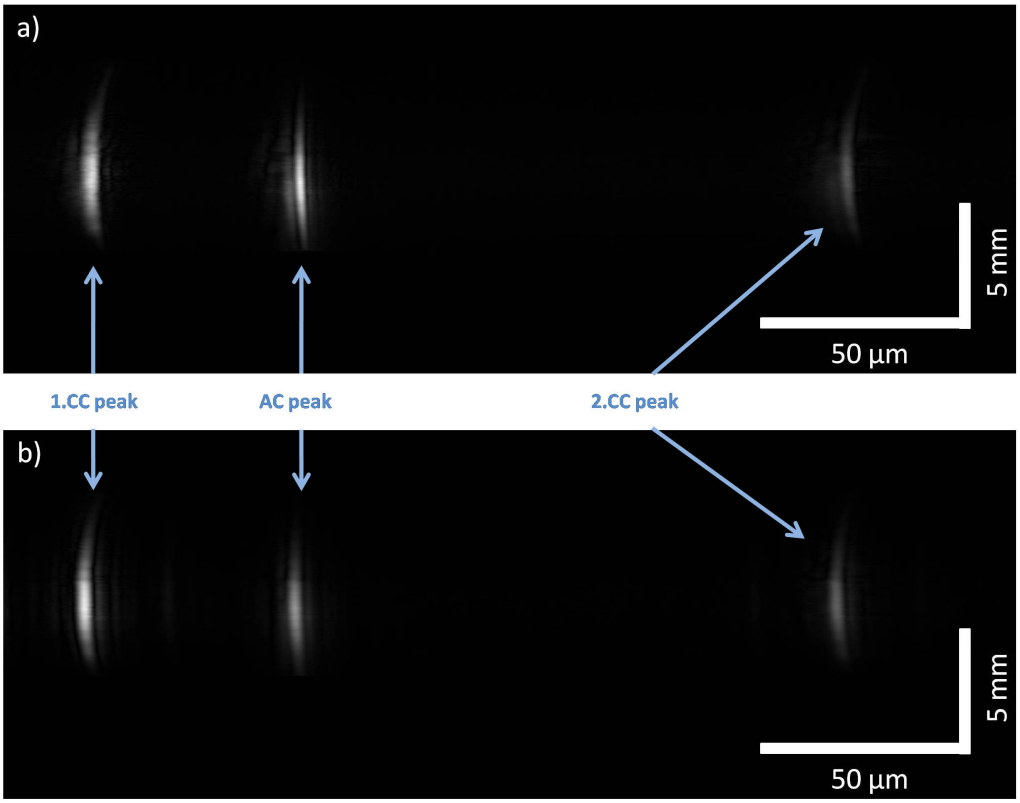

Figure 4.8: 2D tomograms of cover glass obtained with (a) Ti-Sa-Laser and (b) Superlum SLD light source

So far, the system was just tested of its capability of measuring very thin layers around 4 µm (see chapter 4.2.1). Additionally, it was of interest to image reflective layers thicker than the tear film phantoms but still in the range of the maximum imaging depth z_{max}. For that purpose, cover glass plates are a good choice. That is why a cover glass plate with a thickness in the range of 160 to 190 microns as given by the manufacturer (Product No.48393-150, VWR, Pennsylvania, USA) was measured with the setup (see figure 4.8). In figure 4.8, three peaks can be seen. Two of them are located in the first third of the tomogram, where the first one refers to the cross-correlation term of the front reflex of the cover plate (1. CC peak), while the second peak is caused by the auto-correlation interference in the glass plate itself (AC peak). The third peak (2. CC peak) is located at the very back (just above the description of the scale bar) and shows a rather low contrast due to the high sensitivity roll off. This peak can be assigned to the cross-correlation term of the back surface of the cover glass.
The LF-SD-OCT setup performed well and values of 182 µm and 180 µm were obtained by using the Ti-Sa-Laser and the Superlum SLD light source, respectively. Note, that the thickness of the cover glass could be imaged with a higher accuracy than the one of the tear film phantoms. This is due to the fact, that for the cover glass the ratio of the thickness to the measurement error is smaller than for the tear film phantoms.

By comparing the auto-correlation peaks for both light sources, one can see the slightly better resolution of the Ti-Sa-Laser compared to the superlum based on the differences in bandwidth. Furthermore, one can note a dispersive blurring of the cross-correlation peaks compared to the auto-correlation peak.

Chapter 5

Conclusion and Outlook

For this thesis, a complete free space, high-resolution line field spectral domain optical coherence tomography (LF-SD-OCT) setup on a low-cost basis was designed, constructed and characterized. The aim of this project was to design a setup which is not only capable of imaging the human tear film in-vivo but also of evaluating its thickness.

LF-SD-OCT systems are rather inexpensive compared to regular point scanning OCT systems. The overall expenses of the presented system without the light source, yet including all optics, mountings, the detector as well as the connection to the computer are well below 6000 Euro. This is due to the fact, that the system is composed of standard commercially available optical components and can acquire a full two-dimensional depth scan in a single shot. Moreover, the idea of using a low cost interface between the detector and the computer was implemented by using a standard industrial USB-camera.

The main challenge of this low cost free space system is the proper alignment of the optical components, because the positioning and orientation of all lenses has to be very precise to assure good signal quality. This demand has its origin in the design of the free space beam path which becomes even more challenging by the line illumination. The better the lenses are adjusted perpendicular to the incoming beam, the higher is the probability of causing back reflections from the planar surfaces of the optics which are imaged on the detector as well, causing saturation of the camera. Tilting the components was not feasible without introducing severe losses in the interference signal. To avoid saturation issues, the overall power of the light source had to be reduced significantly. In the case of the Ti-Sa-Laser, this led to a very little optical power of only 254 nW measured at the sample, while the maximum allowed power for eye safe operation is around 15 mW for this line field configuration.

With such reduced power, the maximum sensitivity achieved with the Ti-Sa-Laser lies at 73 dB which was measured using a mirror and a neutral density filter in the sample arm. Currently, this low signal is not sufficient for the potential in-vivo imaging of the

tear film. If the maximum allowed power of 15 mW could be used instead, the sensitivity would theoretically gain by 47 dB. Hence, it is realistic to accomplish a sensitivity over 100 dB by reducing or eliminating the back reflections of the optical components.

Reducing these reflections is therefore mandatory for the implementation of in-vivo imaging. One solution could be to use polarization sensitive detection. This can be realized by implementing two linear polarizers (one in the illumination and the other one in the detection arm) perpendicular to each other and two $\lambda/2$-waveplates (one per interferometer arm) rotated by $\pi/8$ to the incident polarization. The polarization filter in the detection arm would then filter out any light reflected from surfaces before the wave plate. Another solution would be to place a slit in the detection arm in a plane conjugated to the sample plane similar to confocal detection. The basic idea is similar to the use of a slit in the setup of Nakamura et al. [25]. They placed a slit right in front of the diffraction grating to suppress the effect of ocular aberrations. However, in the system built and characterized in this thesis, the slit would filter out the unwanted back reflections since it is placed in a plane conjugated to the sample and camera plane.

The axial resolution of the system was measured to be $3.7 \pm 1.0\,\mu m$ when using the Ti-Sa-Laser which is in good accordance with the theoretical value of $2.4\,\mu m$. The resolution is mainly limited by the issue that only approximately 90% of the bandwidth of the Ti-Sa-Laser at its output ($\lambda_0 = 740.5$ nm and a bandwidth of approximately 136.7 nm) is imaged on the camera chip. This is due to the wavelength dependent transmission of different optical components leading to a strong attenuation for wavelengths shorter than 750 nm. The whole setup was planned for a Ti-Sa-Laser with a central wavelength about $\lambda_0 = 800$ nm and a bandwidth of approximately 300 nm. If this spectrum could be achieved, the theoretical axial resolution would be $0.9\,\mu m$ in air and $0.6\,\mu m$ in case of the tear film phantoms. Furthermore, the lateral resolution along the illuminated line was estimated to be at least in the magnitude of $20\,\mu m$ or even better by obtaining sharply resolvable images of a reticle with this line width.

Due to the large bandwidth of the light source, the system is highly sensitive to dispersion mismatch between the sample and reference arm. Besides the optical dispersion compensation (prism pair), which adjustment has to be finely tuned, a digital dispersion compensation algorithm was implemented. The code was able to reduce the blurring of the peak significantly but could not fully compensate the remaining dispersion. However, the algorithm could be improved by advancing the evaluation of the quadratic term or adding a fourth-order term and a higher degree of automation. This could additionally increase the overall axial resolution of the system.

Another approach of LF-SD-OCT suppresses dispersion issues right from the beginning by only using reflective instead of refractive optical components (see [26] and [27]). Moreover, back reflection issues caused by the lenses in the interferometer could be avoided completely by the use of these focusing mirrors. The adjustment of such mirrors would probably be even more challenging than of the lens system used in this thesis

and they could cause some additional image errors (e.g. astigmatism). If these problems could be overcome, this system seems very promising for tear film imaging as well.

Different tear film phantoms with thicknesses between $3.26 - 4.81\,\mu m$ were measured to demonstrate the feasibility of qualifying the thickness of thin films comparable to the one of the human pre corneal tear film. These showed good accordance with thickness measurements using a commercial white light interferometer. Note that these samples are just slightly thicker than the current axial resolution. Hence, their thickness cannot be measured with high accuracy so far, but this can be improved by adjusting the spectral shape of the Ti-Sa-Laser to have a longer central wavelength and a bigger bandwidth just as the spectrum for which the setup was planned. Furthermore, the setups ability of measuring thicker samples was demonstrated with a cover glass plate ($180\,\mu m$ thick, BK7). Overall these first measurements show the high potential of the setup for future in-vivo imaging of the eye's tear film, which is in the range of $3.0 - 6.3\,\mu m$ (see [9] and [10]).

In conclusion, once the back reflections are eliminated, it can be assumed that a high sensitivity up to the current state of the art point scanning OCT systems can be reached, thus, opening the door for in-vivo imaging. The current axial resolution is sufficiently high for resolving a tear film, yet the spectrum of Ti-Sa-Laser could be improved in order to determine the tear film thickness with a higher accuracy, i.e. an axial resolution about $1\,\mu m$.

As soon as the first high resolution in-vivo images could be obtained, the next step will be implementing a scanner for lateral scanning in the dimension perpendicular to the illumination line. This would enable a 3D-visualization of how the tear film is evolving in time as well as where and when it breaks up within the maximum imaging depth.

Appendix A

Theory of Interference and Diffraction

For dimensioning of the spectrometer (see chapter B) it is necessary to know the grating equation and the width of the 1st-order principal maximum which will be discussed in this chapter.

A.1 Diffraction in the sense of interference

In optics diffraction describes the phenomenon that a beam of light, which is limited by an aperture (or edges of any kind of an opaque material) which absorbs or reflects a part of the light beam, may partly get sidetrackted. Hence, light may be detected in some areas, which it could not reach by means of geometrical optics.

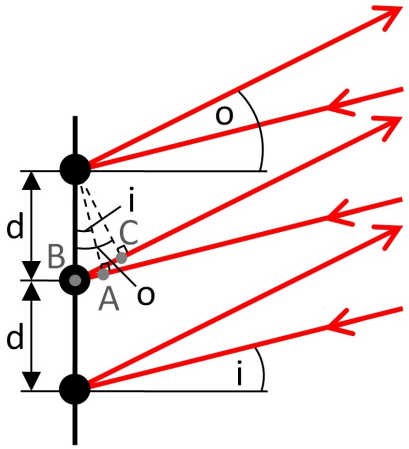

Figure A.1: The geometrics of the total path difference $\Delta s = \overline{AB} + \overline{BC}$ which lead to the phase shift $\Delta\phi$

The black dots in figure A.1 illustrate N periodically placed oscillators along the vertical

axis, whereby d is the distance between two neighbouring oscillators. An incoming wave arrives at the oscillators at the angle i and forces the oscillators to oscillate. As a result, the oscillators emit waves at the angle o.
In order to calculate the total amplitude it is necessary to take into account that the incoming wave does not hit all oscillators at the same time and the emitted partial waves have a path difference. The total path difference Δs between two partial waves emitted from neighbouring oscillators in the plane which is transverse to the emitting direction o may be caculated by using the geometrics of the figure A.1:

$$\Delta s = \overline{AB} + \overline{BC} = d\,(\sin i + \sin o) \tag{A.1}$$

This path difference leads to the phase shift

$$\Delta\phi = k\,\Delta s = \frac{2\pi}{\lambda}\,d\,(\sin i + \sin o) \tag{A.2}$$

All partial waves have the same amplitude A_j, hence the total amplitude of the N oscillators is calculated by

$$E = A \cdot \sum_{j=1}^{N} \mathrm{e}^{i(\omega t + \phi_j)} = A \cdot \mathrm{e}^{i\omega t} \sum_{j=1}^{N} \mathrm{e}^{i(j-1)\Delta\phi}, \tag{A.3}$$

and the phase of the first partial wave is set to be $\phi_1 = 0$.
The sum of the geometric series results in

$$\sum_{j=1}^{N} \mathrm{e}^{i(j-1)\Delta\phi} = \frac{\mathrm{e}^{iN\Delta\phi} - 1}{\mathrm{e}^{i\Delta\phi} - 1} = \mathrm{e}^{i\frac{N-1}{2}\Delta\phi} \cdot \frac{\sin(N\Delta\phi/2)}{\sin(\Delta\phi/2)} \tag{A.4}$$

The intensity $I = c\,\epsilon_0\,|E|^2$ of the total wave in the direction of o results, by using equation A.2, in

$$I(o) = I_0 \cdot \frac{\sin^2(N\Delta\phi/2)}{\sin^2(\Delta\phi/2)} = I_0 \cdot \frac{\sin^2(\frac{N\pi}{\lambda}\,d\,(\sin i + \sin o))}{\sin^2(\frac{\pi}{\lambda}\,d\,(\sin i + \sin o))}, \tag{A.5}$$

where $I_0 = c\,\epsilon_0\,A^2$ is the intensity, emitted by one oscillator.

A.2 Single slit diffraction

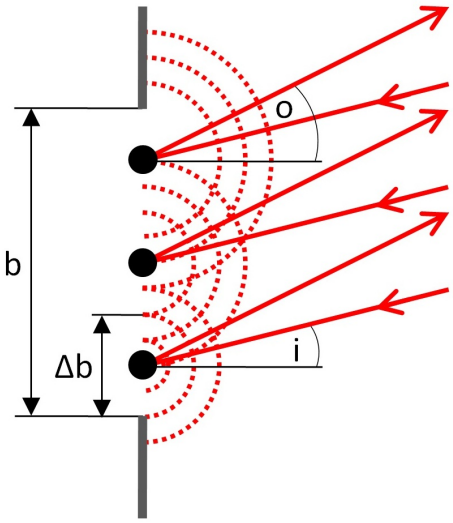

Figure A.2: The geometrics for the derivation of the diffraction at a single slit

A slit with the total width b is divided into N emitting segments with a width of $\Delta b = \frac{b}{N}$. The amplitude of one of these emitting segments is $A = NA_0\frac{\Delta b}{b} \propto \Delta b$. Analogous to chapter A.1, diffraction in the sense of interference, the intensity function is derivated and results in

$$I(o) = I_0\, N^2 \left(\frac{\Delta b}{b}\right)^2 \cdot \frac{\sin^2(\frac{\pi\, N\, \Delta b}{\lambda}\,(\sin i + \sin o))}{\sin^2(\frac{\pi\, \Delta b}{\lambda}\,(\sin i + \sin o))}, \tag{A.6}$$

where I_0 is the intensity emitted by one segment Δb.
For an easier analysis of the behavior of the intensity function, the substitutions $x = \frac{\pi b}{\lambda}(\sin(i) + \sin(o))$ and $\Delta b = \frac{b}{N}$ are used and lead to

$$I(o) = I_0 \frac{\sin^2(x)}{\sin^2(x/N)}. \tag{A.7}$$

Now the number of emitters is maximized $N \to \infty$, i.e. that the width of one emitting segment is minimized $\Delta b \to 0$. That implies $\lim_{N\to\infty} \sin^2(\frac{x}{N}) = \frac{x^2}{N^2}$ and $\lim_{N\to\infty} N^2 I_0 = I_S$, whereby I_S is the total intensity of the slit. Hence equation A.7 simplifies to

$$\lim_{N\to\infty} I(o) = N^2 I_0 \frac{\sin^2(x)}{x^2} = I_S \frac{\sin^2(x)}{x^2} \tag{A.8}$$

Regardless of the value of $\frac{b}{\lambda}$, 90 % of the total incoming luminous power arrives in the central maximum of the diffraction distribution, because of

$$\int_{-\pi}^{\pi} \frac{\sin^2 x}{x^2} \mathrm{d}x = 0,9 \cdot \int_{-\infty}^{\infty} \frac{\sin^2 x}{x^2} \mathrm{d}x \tag{A.9}$$

The first minimum of this function is located at $x = \pi \rightarrow \sin(o) = \frac{\lambda}{b} - \sin(i)$.
For $\sin(o) > \frac{\lambda}{b} + \sin(i)$ exist further maxima, whose amplitudes are decreasing by increasing o.

A.3 Diffraction grating

A diffraction grating splits the incident light up in its different wavelengths. Light incident as a collimated beam on the diffraction grating will be emitted as a collimated beam as well, but at different angles depending on its wavelength components.

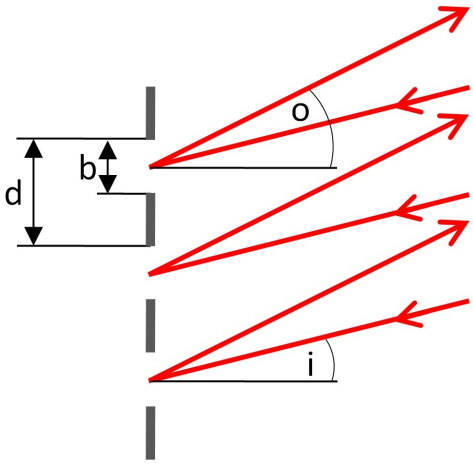

Figure A.3: The geometrics of a reflection diffraction grating

The diffraction grating in figure A.3 is an arrangement of N equally spaced slits or grooves. The intensity function $I(o)$ (see also figure A.4) consists of two terms:

- Interference of the light emitted from different slits (2. fraction in equation A.10)
- Diffraction by every single slit (1. fraction in equation A.10)

$$I(o) = I_S \frac{\sin^2\left[\frac{\pi b}{\lambda}(\sin i + \sin o)\right]}{\left[\frac{\pi b}{\lambda}(\sin i + \sin o)\right]^2} \frac{\sin^2\left[\frac{N\pi}{\lambda} d\,(\sin i + \sin o)\right]}{\sin^2\left[\frac{\pi}{\lambda} d\,(\sin i + \sin o)\right]}, \tag{A.10}$$

where I_S is the passed through intensity of a single slit.

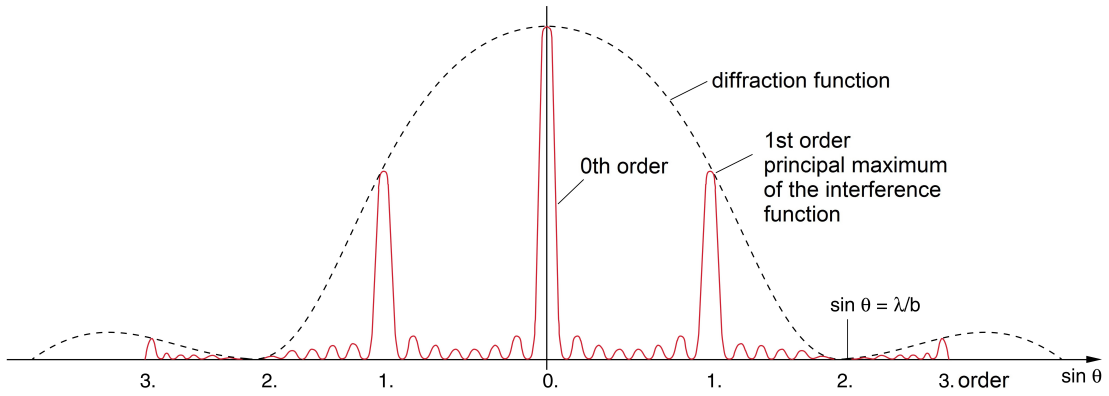

Figure A.4: Intensity distribution $I(o)$ of a diffraction grating with 8 slits, $\frac{d}{b} = 2$ and an incident angle $i = 0$. Due to the minimum of the diffraction function the 2. principal maximum of the interference function cannot be seen. ([28], page 333)

Evaluation of the principal maxima and derivation of the grating equation:

Maxima of the intensity function $I(o)$ occur if the path difference of the emitted light between neighbouring slits $\Delta s = d(\sin(i) + \sin(o)) = m * \lambda$ equals a multiple of the wavelength λ. This leads to the general grating equation:

$$\boxed{\sin(i) + \sin(o) = \frac{m\lambda}{d}} \tag{A.11}$$

where angles that go counterclockwise are positive and those that go clockwise are negative.
The amplitude of these maxima depends on the single slit diffraction and its corresponding factor in equation A.10.
The general grating equation A.11 is necessary in chapter B.1.1 to calculate the required focal lenght of the lens L4 between the diffraction grating and the camera.

Evaluation of the width of the mth-order maximum, i.e. the distance between two neighbouring minima:

For calculation of the distance between two neighbouring minima, the interference term of the equation A.10 can be simplified and then equate to zero:

$$\begin{aligned} \frac{\sin(Nx)}{\sin(x)} = 0 \ , whereby \ \ x = \frac{N\pi}{n} \ , \ n \in \mathbb{Z} \\ \rightarrow \ \frac{\pi}{\lambda} d \, (\sin i + \sin o) = \frac{n\pi}{N} \end{aligned} \tag{A.12}$$

and $d \cdot N$ equals the illuminated "length" at the grating. This leads to the illuminated diameter on the grating D_g

$$d \cdot N = D_g \quad \rightarrow \quad \sin o = \frac{n\lambda}{D_g} - \sin i. \tag{A.13}$$

This equation indicates that all neighbouring minima are equidistant. For reasons of simplification, the following derivation refers to the 0-th principal maximum, but the result is valid for all principal maxima and their zero-crossings.

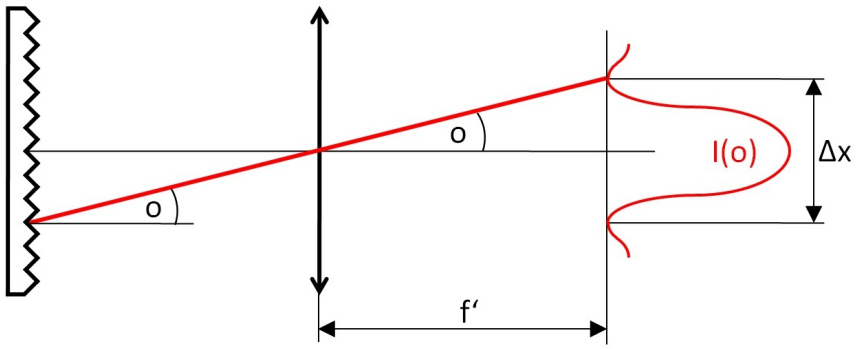

Figure A.5: This figure shows the geometric correlation between the 1. minimum and the related outputangle o at the grating. The double arrow represents the lens, which images the light emitted by the diffraction grating on the camera chip plane.

figure A.5 illustrates the geometrics leading to

$$\tan o = \frac{\Delta x/2}{f'}$$

For small angles between the maximum and the 1. minimum ($n = \pm 1$) applies

$$\sin o \approx \tan o \;\; and \;\; \sin o \approx o$$

The difference between the 1. and the -1. minimum is calculated to be

$$2o \approx \frac{\lambda}{D_g} - \sin i - (\frac{-\lambda}{D_g} - \sin i) = \frac{2\lambda}{D_g}$$

(Note the term $\sin i = const$ drops out by calculating the difference between the 1. and the -1. minimum.)
This leads to

$$\frac{\lambda}{D_g} = \frac{\Delta x}{2f'} \quad \rightarrow \quad \boxed{\Delta x = \frac{2\lambda f'}{D_g},} \tag{A.14}$$

where Δx is the width of the principal maximum, λ is the central wavelength λ_0 of the light source and f' is the focal length of the lens focusing the output of the diffraction grating on the camera chip. Equation A.14 is necessary in chapter B.1.2 to calculate the illuminated diameter on the grating and following this, the required size of the grating and collimator.

Appendix B

Dimensioning of the Spectrometer

The spectrometer was initially planned for the spectrum of a Ti-Sa-Laser with the central wavelength about λ_0 =800 nm and a bandwidth of approx. 300 nm, as shown in figure 3.1. For this purpose the area camera UI-3360CP-NIR-GL (IDS, Obersulm, Germany) with a resolution of 2048 x 1088 pixel was chosen. Although, the cam chip is specially designed for applications in the NIR region, the quantum efficiency decreases with increasing wavelength (see figure 3.9). Therefore, in the selection process of the further components, care was taken that they are very efficient in the high wavelength region.

B.1 Selection criteria for the diffraction grating, the angle of incidence and the lens L4

B.1.1 Optimization of the illuminated area at the camera chip

The whole spectrum of 650 - 950 nm needs to be imaged onto the camera chip and the illuminated area at the camera chip should be as large as possible. The dimensions of the camera chip are 5.984 x 11.264 mm, where the 11.264 is the dimension along the direction of the spectral dispersion, i.e. the horizontal plane in figure 3.4.

In order to fulfill the above requirement, one need to have a closer look of the geometrics of the diffraction grating, the lens L4 and the camera chip in the horizontal plane (see figure B.1).

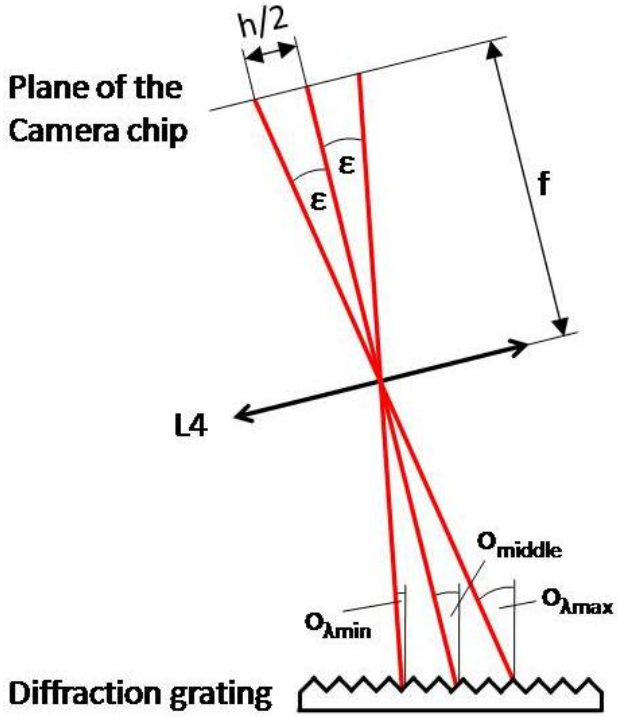

Figure B.1: The used geometric relations for the derivation of f_{max}. The wavelength region from λ_{min} to λ_{max} is the bandwidth of the light source. The two outer red lines are the center rays for the lower and upper end of the bandwidth of the light source. h is the camera chip width in the horizontal plane.

Based on the geometry of figure B.1, the following equations arise:

$$\begin{aligned} o_{middle} &= \frac{o_{\lambda_{min}} + o_{\lambda_{max}}}{2} \\ \epsilon &= 180° - (90° + o_{middle}) - (90° - o_{\lambda_{max}}) = o_{\lambda_{max}} - o_{middle} \\ \tan(\epsilon) \cdot f &\leq \frac{h}{2} \\ \rightarrow f^*_{max} &= \frac{h}{2\tan(o_{\lambda_{max}} - o_{middle})} \end{aligned} \tag{B.1}$$

By this means, the maximum focal length f_{max} of the lens L4 between the grating and the camera can be calculated.
The angles of reflection $o_{\lambda_{max}}$ and $o_{\lambda_{min}}$ are (based on equation A.11) calculated by

$$o_\lambda = \arcsin(\frac{m\lambda}{d} - \sin(i)), \tag{B.2}$$

where by the chosen convention the sign of an angle is measured positive counterclockwise and negativ clockwise. The spacing d between two neighbouring slits of the diffraction grating is the reciprocal of the groove density N [l/mm], hence

$$d\,[mm] = \frac{1}{N\,[l/mm]}.$$

To ensure, that the whole spectrum is imaged on the camera chip, the maximum selectable focal length is multiplied by a factor of 0.9.

$$f_{max} = 0.9 \cdot f^*_{max} = 0.9 \cdot \frac{h}{2\tan(o_{\lambda_{max}} - o_{middle})} \tag{B.3}$$

Based on this equation, several diffraction gratings with different groove densities N are considered and for different angles of incidence i the resulting angle of reflection o and the necessary focal length f_{max} of the lens L4 have been calculated. Possible combinations on the basis of this equation need to fulfill two more criteria. The angle included by the incident and reflected beam must be as large as possible, in order to have enough space for optics and mounting. Moreover, an achromatic lens with the required focal length f_{max} must be commercially available on purchase. Several possible combinations fulfill all this requirements and are listed in table B.1.

For reasons of simplification, the calculations from now on are demonstrated with the values of the finally chosen combination (diffraction grating with 830 l/mm, achromatic lens L4 with a focal length of f=35 mm and the angle of incidence of $i = 70°$). The results for the other combinations are only listed in table B.1, page 64.

B.1.2 Selecting the diffraction grating size and the collimator

In order to select the right collimator and the size of the diffraction grating, the mimimum required beam diamter at the diffraction grating $D_{g,min}$ needs to be calculated.
To reduce spectral crosstalk between neighbouring pixels, the width of the first principal maximum must not be larger than the size of one pixel. For calculating the minimum illuminated beam diameter at the diffraction grating, equation A.14 for the width of the principal maximum is used. With the chosen lens L4 (f=35 mm), the central wavelength of $\lambda_0 = 796\,\text{nm}$ and the pixel size of $\Delta x = 5.5\,\mu\text{m}$, the minimum illuminated beam diameter is calculated by

$$D_{g,min} = \frac{2 \cdot \lambda_0 f}{\Delta x} = \frac{2 \cdot 796\,\text{nm} \cdot 10^{-3} \cdot 35\,\text{mm}}{5.5\,\mu\text{m}} = 10.2\,\text{mm}.$$

In order to have the diffraction grating illuminated at least with the calculated beam diamter $D_{g,min}$ (in der horizontal plane), the incident beam needs to have the minimum diameter $D_{incident,min}$. The diameter $D_{incident,min}$ at the place of the diffraction grating in a plane parallel to lens L3 is equivalent to the beam diameter after the collimator and is calculated by

$$D_{incident,min} = D_{g,min} \cdot \sin(90° - i) = 10.1\,mm \cdot \sin(90° - 70°) = 3.5\,mm.$$

Hence the diffraction grating needs to have at least the dimensions of 10.1 mm along the diffractive direction and 3.5 mm along the direction of reflection only. In the final combination, a diffraction grating with a groove density of 830 l/mm and a size of 25 x 25 mm (product no. 3-2880, Optometrics, Littleton, MA, USA) is chosen.

The collimator 60FC-T-4-M30-02 of the company Schäfter+Kirchhoff (Hamburg, Deutschland) with a focal length of f=30 mm is considered. Assuming that the collimator produces a collimated beam with a Gaussian beam profile, the beam diameter is calculated by ([29], page 3)

$$D_{collimator\ output} = 1.634 \cdot f_{collimator} \cdot \mathrm{NA}_{input\ fiber}.$$

The light is entering the collimator through the fiber SM Hi780 (OZ Optics, Ottawa, Canada). This fiber is based on a Corning HI780 fiber with a NA of 0.14 (Corning, NY, USA). The operating wavelength of this fiber is above 780 nm and the cut off wavelength is less than 750 nm.
Hence the beam diameter after the collimator is calculated to be 6.9 mm and the considered collimator meets the requirement of $D_{g,min}$ in the finally chosen combination and in all the other considered ones listed in table B.1.

B.1.3 Efficiency of the diffraction grating

Another selection criterion is the efficiency of the diffraction grating. Hence efficiency plots of the considered diffraction gratings at the central wavelength of the light source (i.e. approximately 800 nm) and the required angles of incident i were obtained from the companies.

The quantum efficiency of the camera chip is decreasing in the region from 650 nm to 950 nm. Hence, the efficiency of the ideal diffraction grating is high and increasing within this wavelength region.

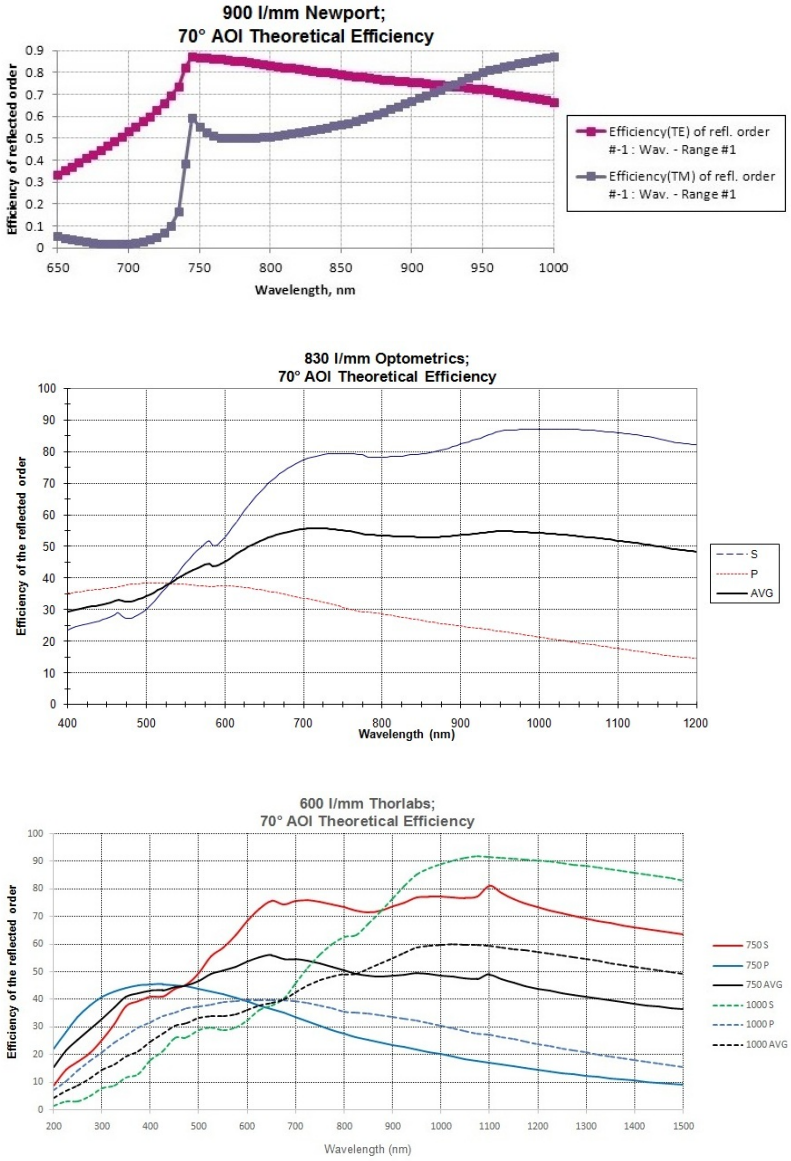

Figure B.2: Theoretical efficiency plots of the considered diffraction gratings. AOI - angle of incidence.

B.1.4 Comparison of different possible combinations

The components of the various manufactures have specific technical characteristics. This leads to several possible combinations with different characteristic values, which yield benefits and difficulties in the result as well as in the positioning as described in the following.

Table B.1: Comparison of different possible combinations of the components of the spectrometer. Different choices of diffraction grating and angle of incidence result in different values of the parameters. The considered parameters are o_{middle} - average angle of reflection, f_{max} - maximum possible focal length of the lens L4, chosen f - focal length of the chosen lens L4, $D_{g,min}$ - minimum illuminated beam diameter at the diffraction in order to reduce spectral crosstalks, and h_{used} - the theoretical illuminated length on the camera chip in the horizontal plane. All mentioned diffraction gratings are reflection gratings. The combination with the diffraction grating of Optometrics is the one which is finally chosen and grey shaded in table.

Used diffraction grating; Angle of incidence	o_{middle} [°]	f_{max} [mm]	chosen f [mm]	$D_{g,min}$ [mm]	h_{used} [mm]
900 l/mm Newport; $i = 70°$	-13	36.3	35	10.2	9.8
830 l/mm Optometrics; $i = 70°$	-16	38.8	35	10.2	9.1
600 l/mm Thorlabs; $i = 70°$	-28	49.7	50	14.5	10.2
600 l/mm Thorlabs; $i = 56°$	-21	52.5	50	14.5	9.7

When comparing the efficiency plots, it is noticeable that in the short wavelength region of 650 - 720 nm the efficiency of the diffraction grating of Newport is only half of the efficiency of the other ones. Therefore the diffraction grating of Newport is neglected in further considerations.
Above 800 nm the efficiency of the diffration grating of Thorlabs (balzed at 750 nm) even decreases with increasing wavelength. Hence, this diffraction grating was neglected as well.
The diffraction grating of Optometrics with a groove density of 830 l/mm is the only diffraction grating of the considered combinations with a high efficiency throughout over 50 %.
The efficiency of the diffraction grating of Thorlabs (blazed at 1000 nm) is in the range of 650 -720 nm less than 50 % and therefore smaller than the efficiency of the one by Opto-

metrics within this region. On the positive side, the efficiency of this diffraction grating increases with increasing wavelength. Hence, this diffraction grating of Thorlabs may compensate the decreasing efficiency of the camera chip in the high wavelength region a bit better than the one of Optometrics.

The positioning of the lens L4 and the camera chip under the desired angle of reflection may be difficult. The closer the theoretical illuminated length at the camera chip h_{used} is to the camera chip dimension of 11.264 mm the more difficult the proper positioning will be.
The final chosen combination with the diffraction grating of Optometrics has a tolerance in proper positioning of the camera chip, which is by 1.1 mm bigger than the one with Thorlabs and an angle of incidence of 70°. The tolerance of the combination with the diffration grating of Thorlabs and an angle of incidence of 56° is only 0.5 mm larger than the combination with the same diffraction grating and an angle of incidence of 70°.
Regarding the practicability of the positioning of the spectrometer, the final combination with the diffraction grating of Optometrics is the most confident realizable combination.
By the first trial assembly, experience in positioning of the lens L4 and the camera was achieved. Consequently the combination with the diffraction grating of Thorlabs and an angle of incidence of 70° would be practical realizable.
Moreover, the lateral resolution increases with an increasing number of illuminated pixels. In this respect, the combination with the diffraction grating of Thorlabs and an angle of incidence of 70° would be better as the one with Optometrics.

A future light source will maybe be a white light source with a typical central wavelength of 850 nm and a wavelength region of approximately 700 -1000 nm. Unfortunately, the efficiency of the camera chip decreases with increasing wavelength even more and at 1000 nm it has already dropped to 5 % (see figure 3.9). The efficiency of the diffraction grating of Optometrics remains high and relatively constant over 50 %. The efficiency of the Thorlabs one (blazed at 1000 nm) is at 700 nm only slightly over 40 %, but increases up to 1000 nm to even 60 %. Hence, the last-named diffraction grating may compensate the decreasing efficiency of the camera chip in the high wavelength region a bit better than the one of Optometrics.

B.2 Results and discussion of the first spectrometer design

With the diffraction grating from Optometrics that was finally chosen for building the spectrometer, 9.1 mm of the full camera chip length of 11.265 mm are illuminated in the direction along the spectral dispersion by the spectrum of the Ti-Sa-Laser. This configuration ensures a good balance between high lateral resolution and practicability of the setup of the spectrometer.
In order to minimize spectral crosstalk between neighbouring pixels, the beam that is illuminating this diffraction grating needs to have a size of at least 10.1 mm along the diffractive direction and 3.5 mm along the direction of reflection. This requirement is realized by the chosen collimator which creates a collimated beam diameter of 6.9 mm. Therewith, the illumination of the diffraction grating has dimensions of 20.2 mm along the diffractive direction and 6.9 mm along the direction of reflection.
The efficiency of the Optometrics-grating remains high and relatively constant over 50 %, over the wide wavelength range 700 - 1000 nm that is suitable for a white light source that might potentially be used with the present optical setup.

As a consequence of the first trial assembly with the Optometrics-grating, experience in positioning of the lens L4 and the camera was achieved. Furthermore, by means of the experiments, knowledge about the potential practicability of using the diffraction grating from Thorlabs with an angle of incidence of 70° was obtained.
The performance of the setup with the Thorlabs-diffraction grating (blazed at 1000 nm) and an angle of incidence of 70° would be a little bit better than the one with the Optometrics-grating. This is due to the fact that the diffraction grating of Thorlabs may compensate the decreasing efficiency of the camera chip in the high wavelength region a bit more than the one of Optometrics. This holds also true for a future setup using a white light source. Moreover, based on the maximized coverage of the camera chip length with the illuminating beam, a higher lateral resolution could be achieved in combination with the diffraction grating of Thorlabs.
The Optometrics-grating was chosen for the final setup due to the fact that it shows comparable performance to the Thorlabs-grating, but enables an easier implementation and alignment of the spectrometer.

In conclusion, taking into account the calculated parameters and the experimental results, the chosen combination with the diffraction grating of Optometrics meets all technical requirements.

Bibliography

[1] B. Grajciar, M. Pircher, A. F. Fercher, and Leitgeb R. A. Parallel Fourier domain optical coherence tomography for in vivo measurement of the human eye. *Optics Express*, 13(4):1131–1137, February 2005. doi: 10.1364/OPEX.13.001131.

[2] The epidemiology of dry eye disease: report of the Epidemiology Subcommittee of the International Dry Eye WorkShop (2007). *The Ocular Surface*, 5(2):93–107, April 2007. ISSN 1542-0124.

[3] Methodologies to diagnose and monitor dry eye disease: report of the Diagnostic Methodology Subcommittee of the International Dry Eye WorkShop (2007). *The Ocular Surface*, 5(2):108–152, April 2007. ISSN 1542-0124.

[4] S. Mishima. Some physiological aspects of the precorneal tear film. *Archives of Ophthalmology (Chicago, Ill.: 1960)*, 73:233–241, February 1965. ISSN 0003-9950.

[5] D. A. Benedetto, D. O. Shah, and H. E. Kaufman. The instilled fluid dynamics and surface chemistry of polymers in the preocular tear film. *Investigative Ophthalmology*, 14(12):887–902, December 1975. ISSN 0020-9988.

[6] N. Fogt, P. E. King-Smith, and G. Tuell. Interferometric measurement of tear film thickness by use of spectral oscillations. *Journal of the Optical Society of America. A, Optics, Image Science, and Vision*, 15(1):268–275, January 1998. ISSN 1084-7529.

[7] J. I. Prydal, P. Artal, H. Woon, and F. W. Campbell. Study of human precorneal tear film thickness and structure using laser interferometry. *Investigative Ophthalmology & Visual Science*, 33(6):2006–2011, May 1992. ISSN 0146-0404.

[8] Tilman Schmoll, Angelika Unterhuber, Christoph Kolbitsch, Tuan Le, Andreas Stingl, and Rainer Leitgeb. Precise thickness measurements of Bowman's layer, epithelium, and tear film. *Optometry and Vision Science: Official Publication of the American Academy of Optometry*, 89(5):E795–802, May 2012. ISSN 1538-9235. doi: 10.1097/OPX.0b013e3182504346.

[9] Rahul Yadav, Kye-Sung Lee, Jannick P. Rolland, James M. Zavislan, James V. Aquavella, and Geunyoung Yoon. Micrometer axial resolution OCT for corneal imaging. *Biomedical Optics Express*, 2(11):3037–3046, October 2011. ISSN 2156-7085. doi: 10.1364/BOE.2.003037. URL http://www.ncbi.nlm.nih.gov/pmc/articles/PMC3207373/.

[10] Ranjini Kottaiyan, Geunyoung Yoon, Qi Wang, Rahul Yadav, James M. Zavislan, and James V. Aquavella. Integrated multimodal metrology for objective and non-invasive tear evaluation. *The Ocular Surface*, 10(1):43–50, January 2012. ISSN 1542-0124. doi: 10.1016/j.jtos.2011.12.001.

[11] René M. Werkmeister, Aneesh Alex, Semira Kaya, Angelika Unterhuber, Bernd Hofer, Jasmin Riedl, Michael Bronhagl, Martin Vietauer, Doreen Schmidl, Tilman Schmoll, Gerhard Garhöfer, Wolfgang Drexler, Rainer A. Leitgeb, Martin Groeschl, and Leopold Schmetterer. Measurement of tear film thickness using ultrahigh-resolution optical coherence tomography. *Investigative Ophthalmology & Visual Science*, 54(8):5578–5583, August 2013. ISSN 1552-5783. doi: 10.1167/iovs.13-11920.

[12] Sang-Won Lee and Beop-Min Kim. Line-field optical coherence tomography using frequency-sweeping source. *IEEE Journal of Selected Topics in Quantum Electronics*, 14(1):50–55, 2008. URL http://ieeexplore.ieee.org/xpls/abs_all.jsp?arnumber=4451123.

[13] Daniel J. Fechtig, Branislav Grajciar, Tilman Schmoll, Cedric Blatter, Rene M. Werkmeister, Wolfgang Drexler, and Rainer A. Leitgeb. Line-field parallel swept source MHz OCT for structural and functional retinal imaging. *Biomedical Optics Express*, 6(3):716, March 2015. ISSN 2156-7085, 2156-7085. doi: 10.1364/BOE.6.000716. URL https://www.osapublishing.org/boe/abstract.cfm?uri=boe-6-3-716.

[14] Wolfgang Drexler and James G. Fujimoto, editors. *Optical Coherence Tomography*. Springer International Publishing, Cham, 2015. ISBN 978-3-319-06418-5 978-3-319-06419-2. URL http://link.springer.com/10.1007/978-3-319-06419-2.

[15] S. Marschall, B. Sander, M. Mogensen, T. M. Jørgensen, and P. E. Andersen. Optical coherence tomography - current technology and applications in clinical and biomedical research. *Analytical and Bioanalytical Chemistry*, 400:2699–2720, May 2011. doi: 10.1007/s00216-011-5008-1.

[16] R. Leitgeb, C. Hitzenberger, and Adolf Fercher. Performance of fourier domain vs time domain optical coherence tomography. *Optics Express*, 11(8):889, April 2003. ISSN 1094-4087. doi: 10.1364/OE.11.000889. URL https://www.osapublishing.org/oe/abstract.cfm?uri=oe-11-8-889.

[17] Michael Choma, Marinko Sarunic, Changhuei Yang, and Joseph Izatt. Sensitivity advantage of swept source and Fourier domain optical coherence tomography. *Optics Express*, 11(18):2183, September 2003. ISSN 1094-4087. doi: 10.1364/OE.11.002183. URL https://www.osapublishing.org/oe/abstract.cfm?uri=oe-11-18-2183.

[18] Andrés F. Zuluaga and Rebecca Richards-Kortum. Spatially resolved spectral interferometry for determination of subsurface structure. *Optics Letters*, 24(8):519, April 1999. ISSN 0146-9592, 1539-4794. doi: 10.1364/OL.24.000519. URL https://www.osapublishing.org/abstract.cfm?URI=ol-24-8-519.

[19] Yan Zhang, Jungtae Rha, Ravi Jonnal, and Donald Miller. Adaptive optics parallel spectral domain optical coherence tomography for imaging the living retina. *Optics Express*, 13(12):4792–4811, June 2005. ISSN 1094-4087.

[20] V. Doblhoff-Dier. *Determination of the Total Retinal Blood Flow Using Fourier-Domain Optical Coherence Tomography and Fundus Imaging*. Dissertation, Medical University of Vienna, 2014. URL http://www.ub.tuwien.ac.at/diss/AC12148983.pdf.

[21] Wolfgang Drexler, Mengyang Liu, Abhishek Kumar, Tschackad Kamali, Angelika Unterhuber, and Rainer A. Leitgeb. Optical coherence tomography today: speed, contrast, and multimodality. *Journal of Biomedical Optics*, 19(7):071412, 2014. ISSN 1560-2281. doi: 10.1117/1.JBO.19.7.071412.

[22] IEC 60825–1 ed3.0, "Safety of laser products – Part 1: Equipment classification and requirements," (2014).

[23] Datasheet of UI-3360cp-NIR-GL. *IDS Imaging Development Systems GmbH*, December 2015. URL https://de.ids-imaging.com/IDS/datasheet_pdf.php?sku=AB00624.

[24] Maciej Wojtkowski, Vivek J. Srinivasan, Tony H. Ko, James G. Fujimoto, Andrzej Kowalczyk, and Jay S. Duker. Ultrahigh-resolution, high-speed, Fourier domain optical coherence tomography and methods for dispersion compensation. *Optics Express*, 12(11):2404, May 2004. ISSN 1094-4087. doi: 10.1364/OPEX.12.002404. URL https://www.osapublishing.org/abstract.cfm?URI=oe-12-11-2404.

[25] Yoshifumi Nakamura, Shuichi Makita, Masahiro Yamanari, Masahide Itoh, Toyohiko Yatagai, and Yoshiaki Yasuno. High-speed three-dimensional human retinal imaging by line-field spectral domain optical coherence tomography. *Optics Express*, 15(12):7103, June 2007. ISSN 1094-4087. doi: 10.1364/OE.15.007103. URL https://www.osapublishing.org/abstract.cfm?URI=oe-15-12-7103.

[26] Mohammad Kamal, Narayanswamy Sivakumar, and Muthukumaran Packirisamy. Design of a spectrometer for all-reflective optics-based line scan Fourier domain

optical coherence tomography. volume 7750, pages 775020–775020–6, 2010. doi: 10.1117/12.873105. URL http://dx.doi.org/10.1117/12.873105.

[27] Mohammad Kamal, Sivakumar Narayanswamy, and Muthukumaran Packirisamy. Design of spectrometer for high-speed line field optical coherence tomography. volume 8007, pages 80071J–80071J–8, 2011. doi: 10.1117/12.905578. URL http://dx.doi.org/10.1117/12.905578.

[28] W. Demtröder. *Experimentalphysik 2, Elektrizität und Optik*. Springer, 2009.

[29] Datasheet of 60fc-T-4-M30-02. *Schäfter + Kirchhoff GmbH*, December 2015. URL http://www.sukhamburg.com/download/fk60fc_e.pdf.